5

Drift Chamber

5.1 Physics Requirements and Performance Goals

The goals of the BaBar experiment require that exclusive final states from B^0 decays be reconstructed efficiently and with high resolution. This places stringent demands on the performance of the main tracking chamber. It must provide maximal solid angle coverage, good momentum resolution at all momenta, and efficient reconstruction of tracks as low as $100\,\mathrm{MeV}/c$. In addition, the tracking chamber provides one of the two major triggers for the experiment. These requirements are met through the use of a small-cell, low-mass drift chamber which, in addition to providing excellent momentum resolution for low-momentum tracks, minimally degrades the performance of the calorimeter and particle identification device.

Figure 5-1 shows the integrated efficiency for a variety of all-charged B decay modes as a function of the momentum and polar angle acceptance. The channels $B^0 \to \pi^+\pi^-$, $B^0 \to J/\psi K^0_S$ with $K^0_S \to \pi^+\pi^-$, and $B^0 \to D^+D^-$ with $D^+ \to K^-\pi^+\pi^-$ have been used in the upper two plots in Figure 5-1 to demonstrate the importance of the forward angle acceptance limit. For example, a factor of 6.5 would be lost in the D^+D^- efficiency if good momentum and particle identification information were not available beyond $\cos\theta = 0.8$. Thus the drift chamber must cover the polar angle range down to the beam-line components in the forward direction, namely 300 mr or $\cos\theta < 0.955$. The backward angle requirement is considerably less stringent. The high- and low-momentum requirements are illustrated in the lower two plots of Figure 5-1; the channel $B^0 \to D^{*+}D^{*-}$, with its subsequent cascade decay $D^{*+} \to \pi^+ D^0$ producing a soft pion, places the greatest demand on the reconstruction of low momentum tracks. The ability to find and reconstruct charged particles down to $100\,\mathrm{MeV}/c$ is clearly required for good efficiency in this mode and in other channels containing one or more D^{*+} mesons.

In order to reconstruct exclusive final states with minimal background, the chamber must provide excellent momentum resolution. For tracks with p above $1\,\mathrm{GeV}/c$, such as those arising from the decay $B^0 \to \pi^+\pi^-$, a resolution of $\sigma_{p_\mathrm{t}}/p_\mathrm{t} \simeq 0.3\% \times p_\mathrm{t}$ is anticipated. For the momentum range 0.1 to $1.0\,\mathrm{GeV}/c$, relevant for tracks from the decay $B^0 \to D^+D^-$, $\sigma_{p_\mathrm{t}}/p_\mathrm{t} \simeq 0.3$–$0.4\%$ should also be achievable. The expected resolution on the reconstructed

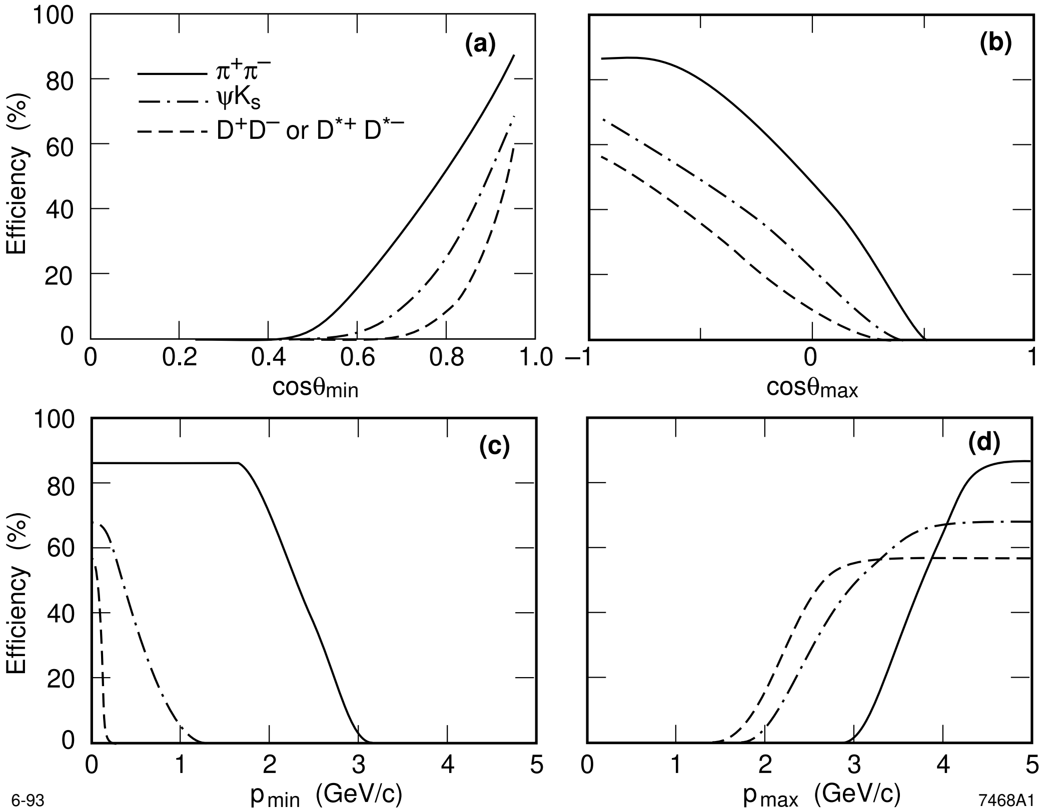

Figure 5-1. *B reconstruction efficiency for charged particle detection from $B^0 \to \pi^+\pi^-$ (solid), $B^0 \to J/\psi K_S^0$, $J/\psi \to \ell^+\ell^-$, $K_S^0 \to \pi^+\pi^-$ (dash-dot), and $B^0 \to D^+D^-$, $D^+ \to K^-\pi^+\pi^+$ for the angular distributions and $B^0 \to D^{*+}D^{*-}$, $D^{*+} \to \pi^+D^0$, $D^0 \to K^-\pi^+$ for the momentum distributions (dashed). Each set of curves is shown as a function of: (a) minimum detectable θ; (b) maximum detectable θ; (c) minimum detectable momentum; and (d) maximum detectable momentum.*

B^0 mass for these decays and the dependence on various drift chamber detector parameters is given in Section 5.3.

At PEP-II, the average charged particle momentum is less than 1 GeV/c. For most particles, the major limitation on track parameter resolution in the drift chamber will be multiple scattering. In order to minimize this effect, the chamber will be made of low-mass materials. A thin inner wall facilitates matching drift chamber and vertex detector tracks, improves the contribution of the high-precision measurement in the outer layer of the SVT to the p_t resolution, and minimizes backgrounds due to photon conversions in the chamber wall. The material in the outer walls and endplates of the chamber must also be kept to a minimum in order to reduce the impact of the drift chamber on calorimeter and particle identification performance.

The drift chamber is expected to participate in the detector trigger by providing one of two complementary trigger streams. The drift chamber must furnish a charged track trigger with a latency of less than $9.5\,\mu$s and a maximum jitter of about $0.5\,\mu$s. The latency constraint results from the buffering in the silicon vertex detector, which therefore requires a strobe at less than 10 kHz. The drift chamber will trigger on one and one-half tracks, *i.e.,* one track traversing the full chamber radius together with one track traversing at least half the chamber radius.

The main tracking chamber serves several other functions as well. For low momentum particles, the chamber will provide particle identification through ionization loss (dE/dx) measurements. For the helium-based gas mixtures under consideration, a resolution of just under 7% should be attainable for the dE/dx measurement, allowing π/K separation up to 700 MeV/c. This capability is complementary to the DIRC in the barrel region, but is essential in the extreme backward direction where no dedicated particle identification device is foreseen.

The drift chamber also allows the reconstruction of secondary vertices, such as decays of K_S^0s outside the silicon detector volume. For this purpose, the chamber should be able to measure not only the transverse coordinate, but also the longitudinal position of tracks with good ($\sim$1 mm) resolution. Good z resolution also aids in matching drift chamber and silicon tracks, and in projecting tracks to the DIRC and calorimeter.

Finally, the chamber must be operational with a margin of safety at the expected backgrounds, which are predicted to be $\sim$5 kHz/cell for the innermost layers. For a five-year period of operation, the integrated charge is expected to be 0.025 C/cm for sense wires in the innermost drift chamber layers, where variations in z and ϕ have been included. Details are described in Chapter 12.

5.2 Tracking Chamber Overview

In order to meet the requirements outlined above, a small-cell drift chamber has been chosen for the *BaBar* detector. Low-Z materials, including a helium-based gas and aluminum wires, will be used in the design. The chamber, illustrated in Figure 5-2, is 280 cm in length and occupies the radial space between 22.5 cm and 80 cm. It is bounded by the support tube at its inner radius and the particle identification device at its outer radius. Forty layers of wires will fill this volume, providing up to 40 spatial and ionization loss measurements for charged particles with transverse momentum greater than 180 MeV/c. Two alternatives have been considered for the wire and layer arrangement: a baseline axial/stereo chamber containing

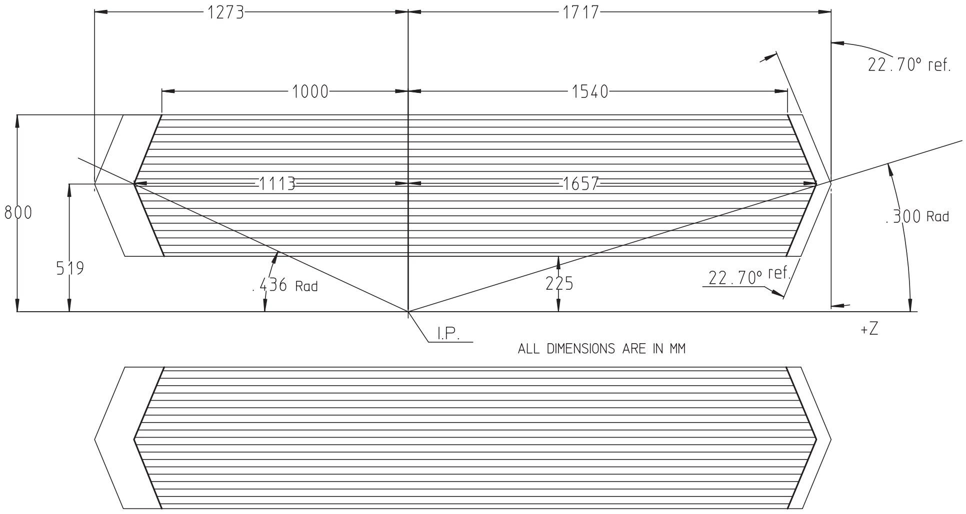

Figure 5-2. *Tracking chamber geometry showing the conical endplates. The chamber is offset in z from the interaction point and extends 1.66 m in the forward direction and 1.11 m in the backward direction. A ten-superlayer structure is indicated. The drift chamber envelope includes a 16 cm space at the backward endcap for readout cards, cables, and an rf-shield. The forward endcap includes a 6 cm space for feedthroughs and an rf-shield.*

four superlayers of axial wires and six superlayers of stereo wires, and an alternative all-stereo chamber containing only layers with positive and negative stereo-angle wires. The wire arrangements are discussed in detail in Section 5.4. For an outer radius of 80 cm, there are about 7000 sense wires of 20 μm-diameter gold-plated tungsten and about 45,000 field wires of 55 μm-diameter gold-plated aluminum. The exact ratio of the number of field to sense wires is still under study.

A chamber length of 166 cm in the forward direction has been chosen. This ensures sufficient coverage for forward-going tracks to avoid compromising the invariant mass resolution, while at the same time does not threaten the electrical stability of the chamber or lead to a prohibitively expensive calorimeter. In the backward direction, a length of 111 cm means that particles with polar angles down to 435 mr penetrate as far as the mid-plane of the chamber, which yields good tracking and dE/dx information.

The endplates, which carry an axial load of 2400 kg, are designed as truncated cones, with the outer part inclined at 22.7° to the vertical. The conic shape provides a substantial increase in mechanical strength and allows particles to enter the forward particle identification device at close to normal incidence. In the forward direction, the tip of the endplate cone lies on the 300 mr line. The inner sections of the endplates will be conically shaped as well. This decreases the wire lengths, permitting larger stereo angles. A detailed comparison of endplate shapes is given in a later section.

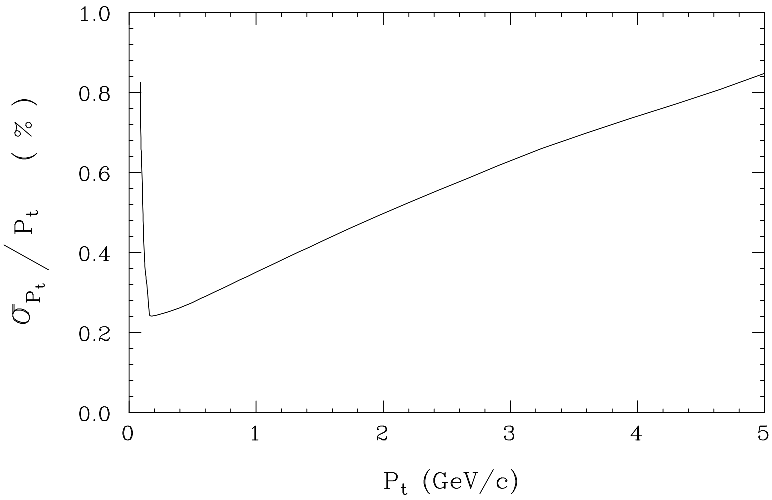

Figure 5-3. *Momentum resolution expected for pions at $\theta = 90°$ for the five-layer silicon vertex detector and the 40-layer drift chamber in a 1.5 T magnetic field. For the drift chamber, an averaged radiation length of 340 m and a single-cell spatial resolution of 140 μm have been assumed. Both the axial/stereo and all-stereo chamber designs give the resolution shown in the figure.*

The inner cylindrical wall of the drift chamber, which sits 15 mm outside the $0.005X_0$ support tube, acts as a gas seal and is not foreseen to provide structural support. The goal is therefore to minimize the inner wall material and the resultant contribution to multiple scattering. To that end, the inner wall will be made out of carbon fiber.

The outer cylindrical wall bears the wire load from the endplates. It is desirable to make this wall as thin as possible, so that the performance of the calorimeter is not degraded. Carbon fiber will therefore be used for the outer wall as well as the endplates.

The chamber will be filled with a helium-based gas at or near atmospheric pressure. In order to minimize the amount of material before the forward endcap, all readout electronics and HV distribution will be placed on the backward endplate.

5.3 Projected Performance

The expected transverse momentum resolution for the five-layer silicon vertex detector and the 40-layer drift chamber in a 1.5 T magnetic field is shown in Figures 5-3 and 5-4. The

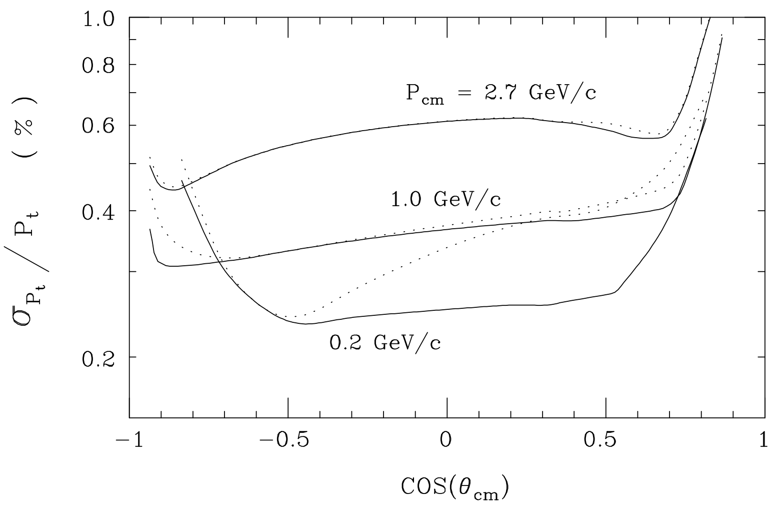

Figure 5-4. *Transverse momentum resolution vs. center-of-mass angle for pions produced with three different center-of-mass momenta. The dotted curves show the total momentum resolution σ_p/p assuming a 100 μm vertex constraint.*

large, low-mass tracking volume provides excellent resolution[1]. For simplicity, a radiation length of 340 m has been used in the calculations: the helium-based gas represents an 800 m radiation length, while the wires, when averaged over space, present a slightly larger amount of material compared to the gas. The inclusion of the effects of discrete wires would result in better chamber performance than that shown. However, systematic effects which would be encountered when reconstructing tracks from actual data have not been included. Such calculations therefore represent the optimal performance of the tracking system, and have been used in a comparative way when exploring various design choices.

Figure 5-4 shows that nearly symmetric forward-backward coverage has been achieved in the center-of-mass frame for momenta above 200 MeV/c. For a He:C_4H_{10} 80:20 gas mixture, with the material from the wires and gas averaged together and with a single-cell spatial resolution of 140 μm, the expected resolution varies from 0.2% for low momentum tracks to 0.5% for high momentum tracks in the central region. The resolution degrades considerably for low-angle tracks, which exit the chamber through the endplates. At low momenta, the total momentum resolution σ_p/p is dominated by the polar angle uncertainty caused by multiple scattering in the silicon. This uncertainty can be significantly reduced by using the primary vertex to impose a constraint on the track. Conservatively assuming the vertex resolution to be 100 μm yields the dotted σ_p/p curves shown in Figure 5-4. At momenta above 1 GeV/c, however,

[1] The calculations were performed using the TRACKERR [Inn93] package, which employs the Kalman-filter technique to analytically propagate the error matrix. The simulation assumes an average 140 μm single cell resolution and multiple scattering contributions from the drift chamber gas and wires.

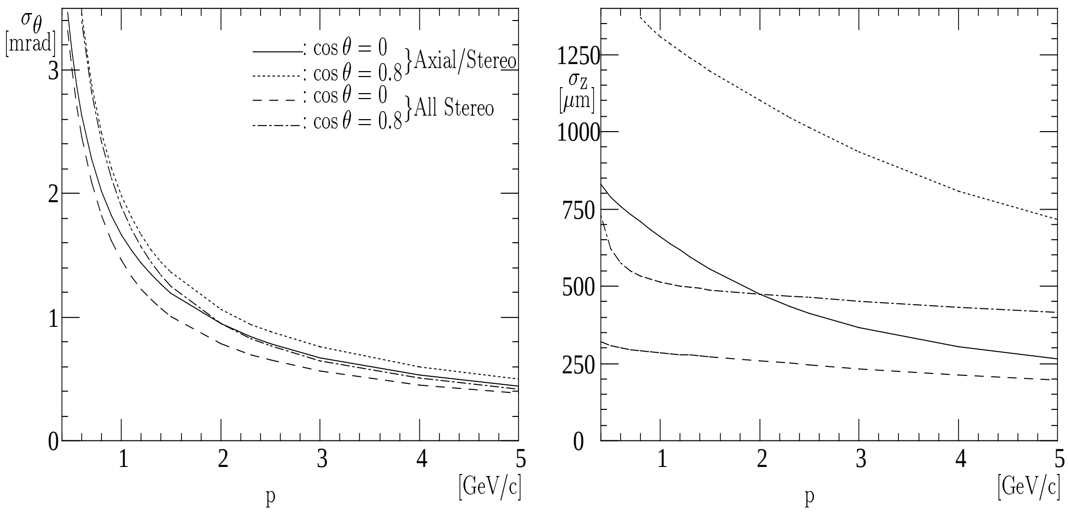

Figure 5-5. *Expected angular resolution (left) and expected z resolution, both at the DIRC, for two different polar angles and for the two chamber configurations.*

the error in the transverse component dominates the total momentum resolution. The z position and polar angle resolutions at the DIRC are shown in Figure 5-5 for various momenta and polar angles. These estimates were obtained using a modified version TRACKERR to simulate the effect of propagating errors outward in the drift chamber to the DIRC radius.

In optimizing the performance of the tracking system, a number of global design parameters have been examined. Neglecting material, the transverse momentum resolution is directly proportional to the single-cell spatial resolution and inversely proportional to the square root of the number of measurements, to the magnetic-field strength, and to the square of the measured arc length in the transverse plane. However, for most momenta encountered in this experiment, multiple scattering in the material within the tracking volume is also an important factor, dominating the resolution below 0.5 GeV/c. The range of mass resolutions which could be provided by the tracking system is illustrated in Table 5-1. It would be tempting to enlarge the radius of the drift chamber beyond 80 cm. However, this is a very expensive direction for design change, since it also drives the volume of CsI required for the calorimeter. Removing the PEP-II support tube is an equally expensive way to improve tracking resolution, since it leads to a much higher risk of reduced luminosity from the machine. This has left magnetic field strength as the most cost-effective way to obtain suitable B mass resolution for CP studies.

Outer Radius (cm)	Support-Tube	Gas-Wires	Resolution (μm)	B Field (Tesla)	Mass Resolution (MeV/c^2) $B^0 \to \pi^+\pi^-$	$B^0 \to D^+D^-$
80	Yes	He-Al	140	<u>1.0</u>	30.7 ± 0.3	5.69 ± 0.09
80	**Yes**	**He-Al**	**140**	**1.5**	$\mathbf{20.8 \pm 0.2}$	$\mathbf{4.70 \pm 0.08}$
80	<u>No</u>	He-Al	140	1.5	17.1 ± 0.1	4.37 ± 0.08
<u>95</u>	Yes	He-Al	140	1.5	14.0 ± 0.1	4.07 ± 0.07
<u>95</u>	<u>No</u>	He-Al	140	1.5	12.5 ± 0.1	3.73 ± 0.06
80	Yes	<u>Ar-Cu</u>	140	1.5	25.2 ± 0.2	5.76 ± 0.09
80	Yes	He-Al	<u>210</u>	1.5	26.0 ± 0.2	5.09 ± 0.09

Table 5-1. *The effect of chamber parameters on mass resolution for $B \to \pi^+\pi^-$ and $B \to D^+D^-$. The entries in bold represent the parameters of the baseline design. The underlined values denote a variation with respect to the baseline. The cases with no support tube are unrealistic to the extent that the effects of a finite thickness for the drift chamber inner wall are not considered.*

5.4 Drift System Design

5.4.1 Cell Design

The drift chamber uses small cells arranged in 40 concentric layers about the axis of the chamber. We have chosen a rectangular cell shape, approximately 13 mm by 19 mm along the radial and azimuthal directions, respectively. In the baseline arrangement, drift cells are arranged in superlayers with either an axial or stereo orientation.

Each cell has one sense wire surrounded by a rectangular grid of field wires, as shown in Figure 5-6. The sense wires are made of gold-coated tungsten, 20 μm in diameter, tensed with a weight of 50 g. The deflection due to gravity is 120 μm at the mid-length of the longest wires. Wire lengths vary from 2.6 m to 2.8 m, due to the conic shape of the end plates. Approximately +1.8 kV is applied to the sense wires with the field wires at ground potential, giving an avalanche gain of approximately 5×10^4.

The field wires are gold-coated aluminum with a diameter of 55 μm. This diameter is sufficiently large to keep the electric field on the wire surface below 20 kV/cm, in order to avoid whisker growth on the wires. A tension of 53 g is applied to the field wires to match the gravitational sag of the sense wires. This tension is roughly one-half the yield tensile strength of the wire.

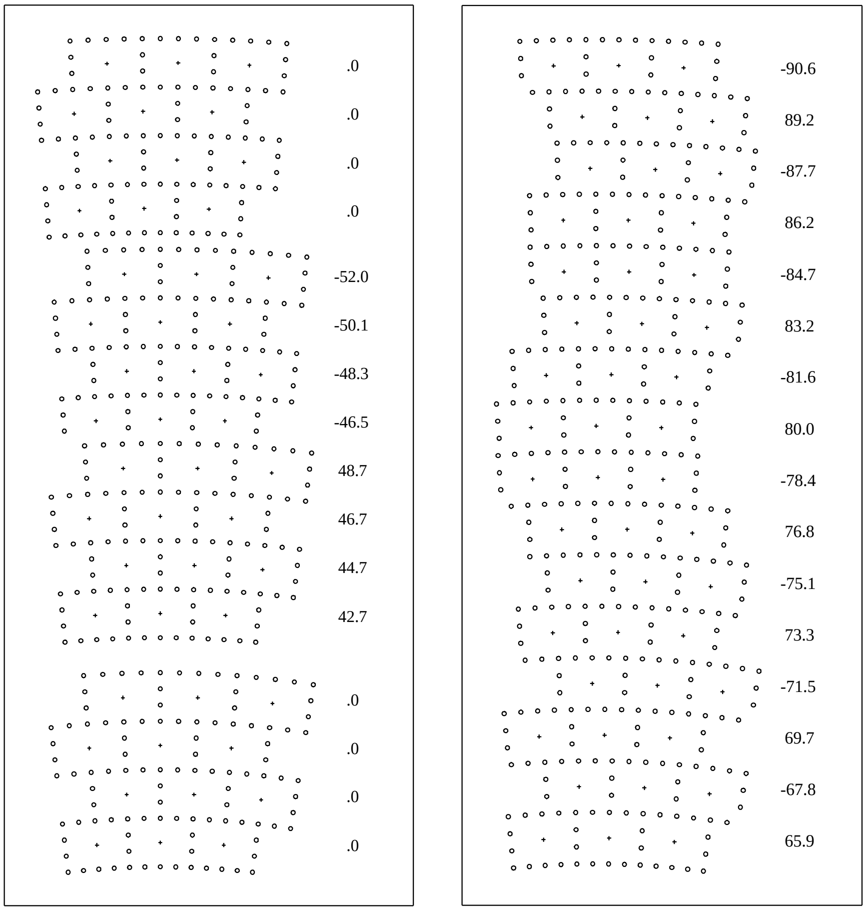

Figure 5-6. *Layers of rectangular cells grouped into axial-stereo (left plot), and all stereo (right plot) configurations. The axial-stereo case has four layers of cells per superlayer and an extra layer of field wires at each axial-stereo boundary to enclose the cells. In the all-stereo case, the layers alternate between positive and negative stereo angles. The stereo angles (mr) of the layers are also shown for each case.*

5.4.2 Layer Arrangement

Two different configurations of wire layers are being considered (Figure 5-6). The baseline configuration has both axial (A) and stereo (U and V) superlayers, while an optional layout having only stereo layers that alternate with positive and negative angles from layer to layer has also been studied.

Axial-Stereo Layer Arrangement

The baseline version of the chamber layout contains ten superlayers with four layers per superlayer. The layers within each superlayer have the same cell count, with cells staggered by half a cell from one layer to the next. This provides a constant cell pattern at all azimuthal angles, which allows local segment finding and left-right ambiguity resolution within a superlayer. The stereo angles of the superlayers alternate between axial (A) and stereo (UV) pairs, in the order AUVAUVAUVA, as shown in Figure 5-6. The difference between the minimum and maximum cylindrical radius of a stereo-layer is known as its stereo sagitta. For each UV pair of superlayers, a stereo sagitta of 5.5 mm is chosen at the innermost layer. This sets the stereo angle for the inner layer, while stereo angles in the other layers of the UV pair are determined by requiring that the wires have the same twist angle (the change in azimuthal angle over the length of the wire) to preserve the cell shapes along the wires. The tangent of the stereo angle varies as the square root of the layer radius within the UV superlayers.

The charged track trajectories in the magnetic field appear circular in the axial views. Three of the five track parameters (the curvature κ, azimuthal angle ϕ, and distance to origin r_0) can be determined from a circle fit in the axial view, while the z position and polar angle θ are determined using the stereo layers. The hardware trigger performs a fast transverse momentum determination using only the axial layers for tracks traversing a significant portion of the chamber. The cell widths for layers in the innermost superlayer vary by $\pm 7\%$, requiring separate time-distance relationships for each layer. This variation decreases at larger radii. Because of the hyperboloidal geometry of stereo layers, the radial space between layers at an axial-stereo boundary varies along the wire, so an extra enclosing layer of field wires is added at the boundaries to provide cell shape uniformity. These additional field layers introduce 5 mm of dead space at six axial-stereo boundaries. A bias voltage of 230 V is applied to the corner field wires in the enclosing layers to sweep out the ions in the dead regions. Table 5-2 gives the radii and stereo angles of all the layers.

The 5 mm enclosing space and the 5.5 mm stereo sagitta result in 10.5 mm radial regions of free space at three radial locations on the end plates, which are otherwise fully populated with feedthroughs. This space may be used to our advantage for gas ports and mechanical stand-offs for cable supports.

All-Stereo Layer Arrangement

The all-stereo optional layout also has 40 layers, but with alternating positive and negative stereo angles. The cell width is nearly constant in all layers, with the cell count increasing by five from one layer to the next layer outward in radius. This constant cell size throughout the whole chamber allows (to first order) a single time-distance relationship to be used for

Layer	Number of cells	Radius at $z = 0$ (mm)	Radius at $z = 1380$ (mm)	Twist (mrad)	Stereo (mrad)	Cell Width (mm)
1	90	241.8	241.8	.0	.0	16.9
2	90	254.4	254.4	.0	.0	17.8
3	90	266.9	266.9	.0	.0	18.6
4	90	279.5	279.5	.0	.0	19.5
5	108	297.0	302.6	386.0	42.0	17.3
6	108	309.3	315.2	386.0	43.8	18.0
7	108	321.7	327.7	386.0	45.5	18.7
8	108	334.0	340.3	386.0	47.3	19.4
9	126	347.3	352.9	-356.8	-45.3	17.3
10	126	359.7	365.5	-356.8	-47.0	17.9
11	126	372.0	378.0	-356.8	-48.6	18.6
12	126	384.4	390.6	-356.8	-50.2	19.2
13	144	408.2	408.2	.0	.0	17.8
14	144	420.8	420.8	.0	.0	18.4
15	144	433.3	433.3	.0	.0	18.9
16	144	445.9	445.9	.0	.0	19.5
17	162	463.4	469.0	308.7	52.2	18.0
18	162	475.8	481.6	308.7	53.6	18.5
19	162	488.3	494.1	308.7	55.0	18.9
20	162	500.7	506.7	308.7	56.4	19.4
21	180	513.7	519.3	-293.1	-54.9	17.9
22	180	526.2	531.9	-293.1	-56.2	18.4
23	180	538.6	544.4	-293.1	-57.6	18.8
24	180	551.0	557.0	-293.1	-58.9	19.2
25	198	574.6	574.6	.0	.0	18.2
26	198	587.2	587.2	.0	.0	18.6
27	198	599.7	599.7	.0	.0	19.0
28	198	612.3	612.3	.0	.0	19.4
29	216	629.8	635.4	264.7	60.7	18.3
30	216	642.3	648.0	264.7	61.9	18.7
31	216	654.8	660.5	264.7	63.1	19.0
32	216	667.2	673.1	264.7	64.3	19.4
33	234	680.1	685.7	-254.7	-63.0	18.3
34	234	692.6	698.3	-254.7	-64.2	18.6
35	234	705.1	710.8	-254.7	-65.3	18.9
36	234	717.6	723.4	-254.7	-66.5	19.3
37	252	741.0	741.0	.0	.0	18.5
38	252	753.6	753.6	.0	.0	18.8
39	252	766.1	766.1	.0	.0	19.1
40	252	778.7	778.7	.0	.0	19.4

Table 5-2. *Radii and stereo angles of all layers in the axial-stereo chamber.*

all the cells. The allowed stereo sagitta of 15 mm determines the stereo angles for each layer, for fixed length wires. The stereo angles range from 66 to 115 mr, from the inner to the outer layer. The layer arrangement is shown in Figure 5-6. Table 5-3 gives the radii and stereo angles of all layers. Alternative arrangements with as few as 36 layers could be considered in this layout. Likewise, consecutive layers could be arranged as superlayers with the same cell count and stereo angle, by sacrificing a small amount of cell uniformity.

Each stereo view has 20 equally spaced layers in the baseline design. In this geometry, tracks are found in each of the views using local-continuity algorithms. For tracks with large curvature, or where overlaps occur, this geometry may be advantageous. Given the projected resolutions in azimuthal angle ϕ and curvature κ, the probability of confusion in matching the two views is small due to the relatively low density of tracks in an $\Upsilon(4S)$ event. Cell widths in this design vary over the length of the chamber by a maximum of $\pm 3\%$ for the innermost layer, decreasing towards larger radii. The cell height in the radial direction is constant.

5.4.3 Total Channel Count

The total channel count in either of the internal layout schemes described above depends on the choice for the total number of layers in the chamber, the channel increment from one layer to the next (or from one superlayer to the next), and the number of channels assigned to the first layer of the chamber. The number of options for these three design parameters is quite limited, as shown in Table 5-4.

The choice of 40 layers is mandatory for an axial-stereo layout. This allows four axial superlayers to complete the primary function of providing a p_{t} measurement, along with three pairs of UV stereo superlayers (with just 12 layers per view). Four layers per superlayer allow three-out-of-four majority logic for triggering and offline segment finding. In principle, the all-stereo design would allow a reduction to as few as 36 layers; this would then be comparable to the ARGUS drift chamber, but with only two rather than three views.

The cell aspect ratio, *i.e.,* ratio of width to height, is defined by the choice of the increment in the cell count, Δ_i, from one layer to the next in proceeding radially outward. In the case of a superlayer design, the cell count is kept fixed for four and is then increased by 4Δ. The simplest designs keep $\Delta_i = \Delta$ fixed over the entire chamber, leading to a uniform cell size. Choosing $\Delta = 6$, as has been used for both ARGUS and CLEO II, produces a nearly square cell in cross section. This is well-suited to the low average momentum in $\Upsilon(4S)$ decays, which results in large angles of incidence on the drift cells with respect to the radial direction. The nearly circular isochrones which dominate a large fraction of the drift-cell response for a square cross section are optimal for handling such arbitrary entrance angles.

Layer	Number of cells	Radius at $z = 0$ (mm)	Radius at $z = 1380$ (mm)	Twist (mrad)	Stereo (mrad)	Cell Width (mm)
1	80	242.2	258.7	718.2	65.8	19.0
2	85	255.5	272.0	-700.2	-67.5	18.9
3	90	268.8	285.3	683.5	69.2	18.8
4	95	282.1	298.6	-667.9	-70.8	18.7
5	100	295.5	312.0	653.4	72.4	18.6
6	105	308.8	325.3	-639.7	-74.0	18.5
7	110	322.1	338.6	626.9	75.5	18.4
8	115	335.4	351.9	-614.8	-77.0	18.3
9	120	348.8	365.3	603.4	78.5	18.3
10	125	362.1	378.6	-592.6	-79.9	18.2
11	130	375.4	391.9	582.4	81.4	18.1
12	135	388.7	405.2	-572.7	-82.8	18.1
13	140	402.1	418.6	563.4	84.1	18.0
14	145	415.4	431.9	-554.6	-85.5	18.0
15	150	428.7	445.2	546.2	86.8	18.0
16	155	442.0	458.5	-538.2	-88.1	17.9
17	160	455.4	471.9	530.5	89.4	17.9
18	165	468.7	485.2	-523.1	-90.7	17.8
19	170	482.0	498.5	516.0	91.9	17.8
20	175	495.3	511.8	-509.2	-93.1	17.8
21	180	508.7	525.2	502.7	94.4	17.8
22	185	522.0	538.5	-496.4	-95.6	17.7
23	190	535.3	551.8	490.3	96.7	17.7
24	195	548.6	565.1	-484.5	-97.9	17.7
25	200	562.0	578.5	478.8	99.1	17.7
26	205	575.3	591.8	-473.4	-100.2	17.6
27	210	588.6	605.1	468.1	101.4	17.6
28	215	601.9	618.4	-463.0	-102.5	17.6
29	220	615.3	631.8	458.1	103.6	17.6
30	225	628.6	645.1	-453.3	-104.7	17.6
31	230	641.9	658.4	448.7	105.7	17.5
32	235	655.2	671.7	-444.2	-106.8	17.5
33	240	668.6	685.1	439.8	107.9	17.5
34	245	681.9	698.4	-435.6	-108.9	17.5
35	250	695.2	711.7	431.5	110.0	17.5
36	255	708.5	725.0	-427.5	-111.0	17.5
37	260	721.9	738.4	423.6	112.0	17.4
38	265	735.2	751.7	-419.8	-113.0	17.4
39	270	748.5	765.0	416.1	114.0	17.4
40	275	761.8	778.3	-412.5	-115.0	17.4

Table 5-3. *Radii and stereo angles of all layers in the all-stereo chamber.*

N_{layers}	N_1	Δ	w/h Ratio	w (cm)	Total Channels	Comments
40	90	(18)/4	1.343–1.550	1.69–1.95	6840	Axial-Stereo Design
	80	5	1.308–1.429	1.74–1.90	7100	All-Stereo Design
40	72	4	1.571	2.15	6000 (5760)	
	90	5	1.257	1.72	7500 (7200)	
	108	6	1.047	1.43	9000 (8640)	Ideal
36	65	4	1.571	2.39	4860	
	82	5	1.257	1.91	6102	All-stereo Option
	98	6	1.047	1.59	7308	All-stereo Option
36	60	6	1.047	1.88	5940	ARGUS
51	96	6	1.047	1.50	12240	CLEO II

Table 5-4. *Total channel counts for the baseline drift chamber designs, compared with various alternative solutions with different numbers of layers (N_{layers}), cell aspect ratios (w/h) as derived from possible layer-to-layer cell increments (Δ), or first-layer channel counts (N_1). The total channel counts in parentheses are for an axial-stereo design, with a four-layer constant-channel superlayer structure.*

The present designs for the *BaBar* chamber compromise on the choice of layer increment in two ways: (1) by choosing to vary Δ slightly from one layer to the next, and (2) by deviating significantly from the ideal square-cell design. Drift cell simulations have shown that increasing the w/h ratio beyond $\sim$1.65 begins to result in performance degradation. The drift cells in either of our design layouts are distinctly rectangular, with the width being 30–55% larger than the height. These are already close to the maximum feasible for good performance in the $\Upsilon(4S)$ environment, as shown in Figure 5-7, leaving little room for additional reduction in channel count.

The last parameter to be considered is the number of cells in the first layer of the chamber. Here, the robustness of the inner layers of the chamber with respect to occupancy is of primary concern. The design choice for *BaBar* lies midway between ARGUS and CLEO II, despite the fact that circulating beam currents in PEP-II will be about 50 times larger than at DORIS II. The ARGUS value was chosen to accommodate the charged multiplicity in $\Upsilon(4S)$ decays. At *BaBar*, considerable effort has been made to understand and control beam-related backgrounds. However, the potential for higher rates has led to a conservative choice of $N_1 = 80$ or 90 in our design.

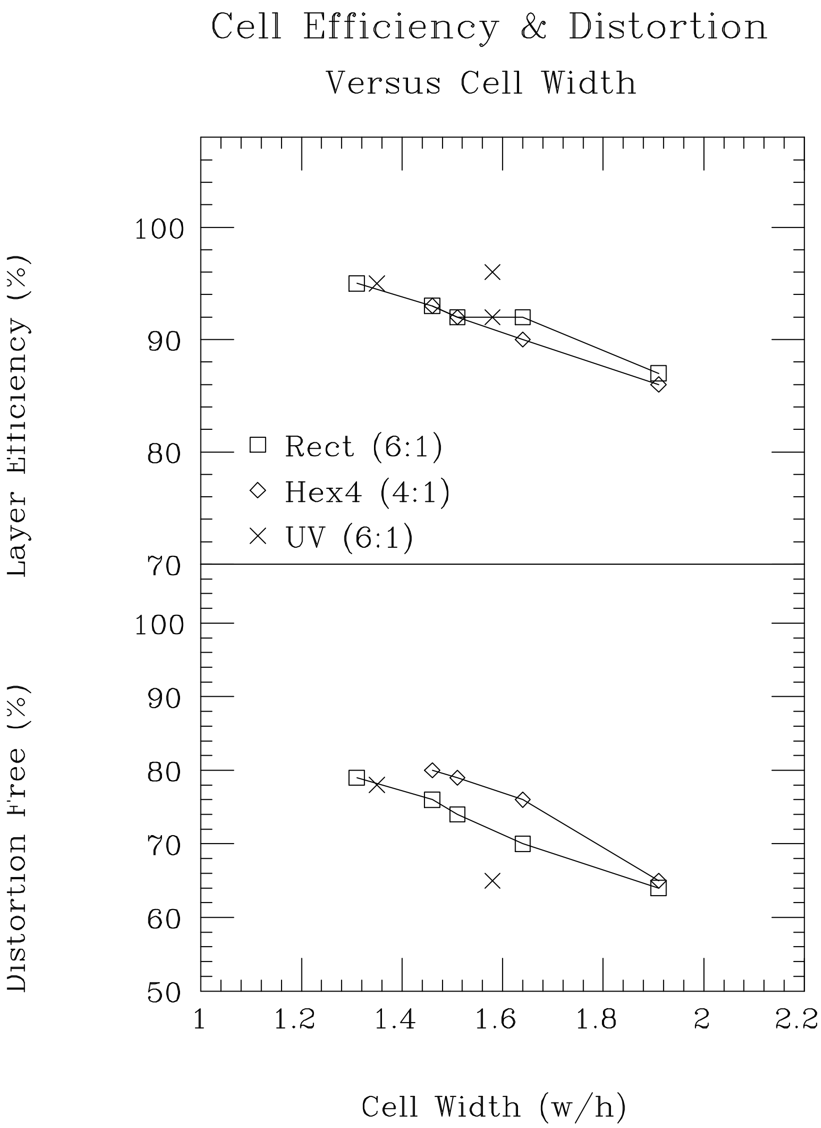

Figure 5-7. *Layer efficiencies (upper) and distortion free regions (lower) as a function of the cell width. Layer efficiencies account for cases where 2 adjacent cells in a layer contain information. Distortion free is defined to be cases with less than 100 μm corrections for angle of incidence.*

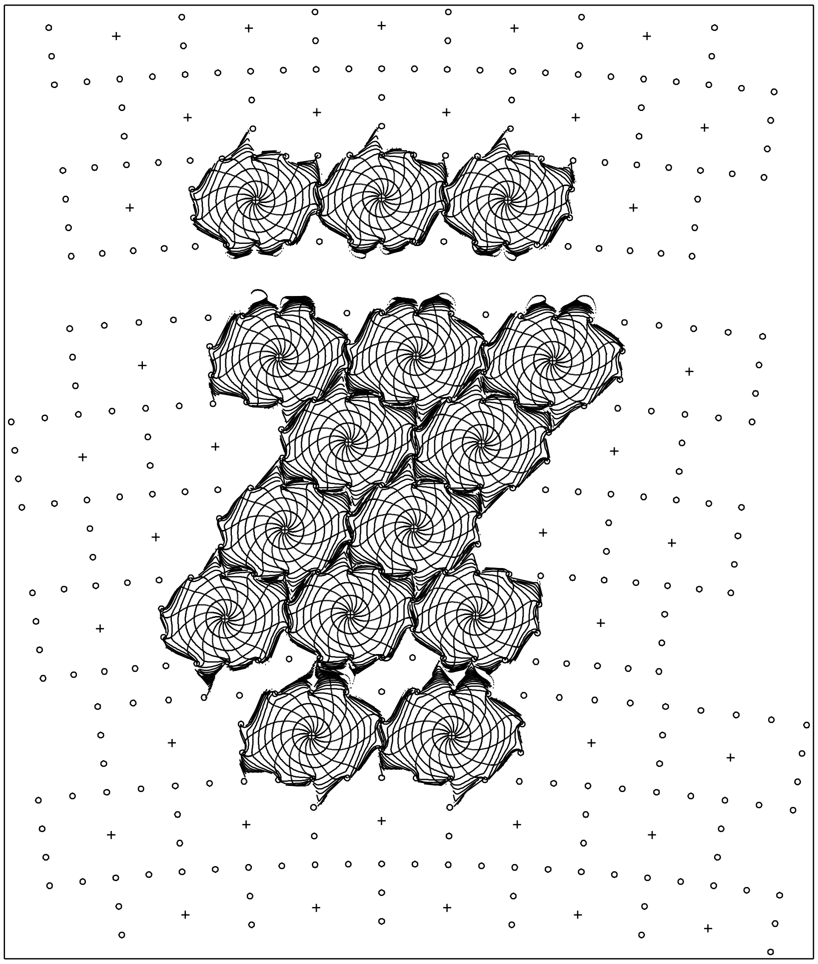

Figure 5-8. *Isochrones for rectangular cells in superlayers. An endplate view is shown of the stereo layers on either side of a four-layer axial superlayer, with enclosing field wires. A 230 V potential on the cell's corner wires in the enclosing layers clears out the ions between these layers. The plots show equal drift time contours at 100 ns intervals.*

5.4.4 Cell Studies

A simulation package (DCSIM), which models drift chamber responses to charge deposition for given wire configurations, has been used to study various cell properties, including drift time isochrones, time-distance relationships, distortions, and gain variations.

Isochrones for the rectangular cells in axial-stereo superlayers are shown in Figure 5-8. A similar plot for the all-stereo design is shown in Figure 5-9. The cells have circular contours near the sense wire but become distorted near the field wires. In the superlayer case, a

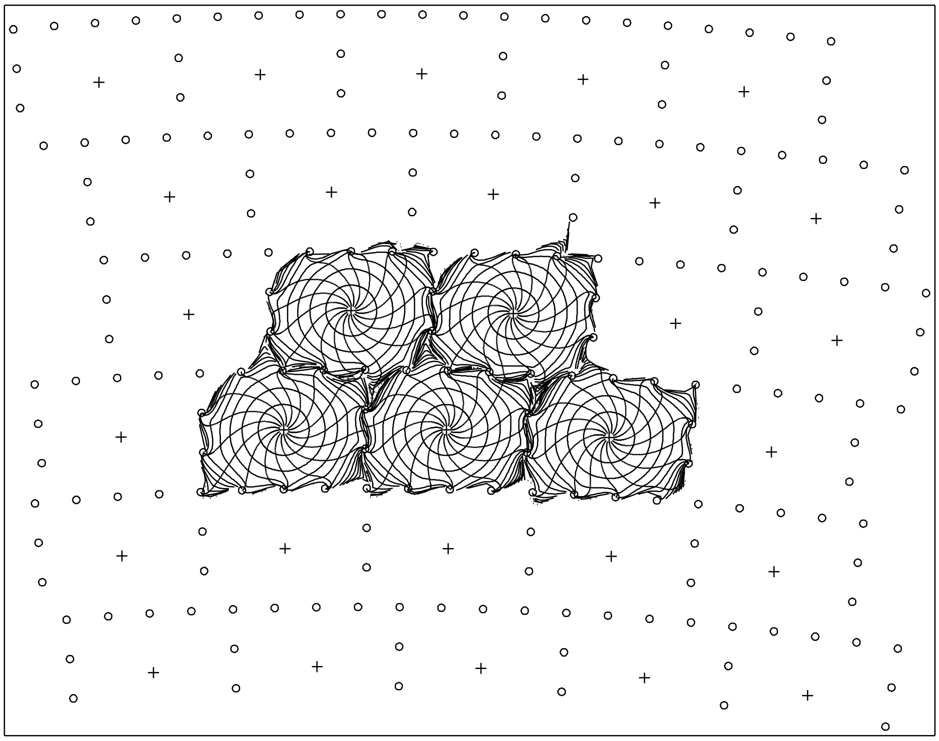

Figure 5-9. *Isochrones for all-stereo cells. The plots show equal drift time contours at 100 ns intervals.*

potential of +230 V at the cell corners in the enclosing layers clears out the electrons in the dead space between these enclosing layers.

Although isochrones show drift times of electrons anywhere in the cell, they do not easily describe the collection of electrons originating along tracks. The time-distance relationship of tracks in small cells has been simulated and compared with measurements made with the Prototype I chamber. The simulation program generates tracks and computes the average drift time of electrons over a short track segment centered about the minimum arrival point. The length of a short segment used in the simulation was made equal to the mean free path between primary electrons. Figure 5-10 shows the agreement between the simulated time-distance curves and measurements in Prototype I with an 80:20 mixture of He:C_4H_{10} gas.

These simulated time-distance relationships have then been used to study other cell properties. The time-distance dependence on the track entrance angle has been calculated, along with the distortions which would arise if a single time-distance function were used over a range of track angles. For each drift time in a cell the track distance from the wire at various

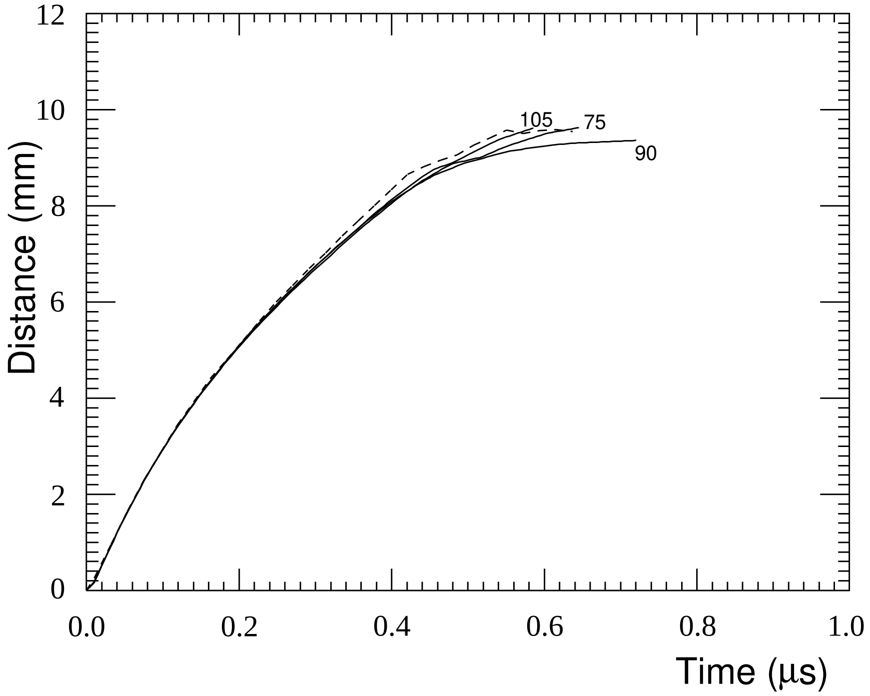

Figure 5-10. *Simulated and measured time-distance functions. The solid curves are the simulated time-distance curves for track angles of 75, 90, and 105°, where 90° is along the radial direction. Measurements in a prototype chamber with no magnetic field are shown by the dashed curve.*

track angles is calculated, and the average and rms spreads in distance over a range of track angles are determined. The rms spread is a measure of the distortion that a single time-distance function would have due to the effects of track angles in the cell. Figure 5-11 shows the rms spread in distance over track angles within $\pm 30°$ of the radial direction for the four layers within a superlayer. The left plot has all field wires at ground potential, while the right plot has compensated voltages of $+230$ V at cell corners on enclosing layers and -120 V on the pairs of wires between the sense wires. The distortions are smaller in the latter case. One can compare distortions for various cell geometries by recording the distance of closest approach (DCA) at which the rms variation is $100\,\mu$m. For the rectangular cell shown, this is at 7.4 mm for vertical tracks, which is 78% of the 9.5 mm geometric half-width of the cell. Table 5-5 shows the distance of closest approach values at the distortion limit of $100\,\mu$m for various cell and layer geometries.

The spatial resolution has been determined for those parts of the cell in which a sufficient number of electrons is collected within the leading edge of the signal, defined to be the case in which two electrons arrive within 10 ns of the theoretical minimal drift time. The DCA

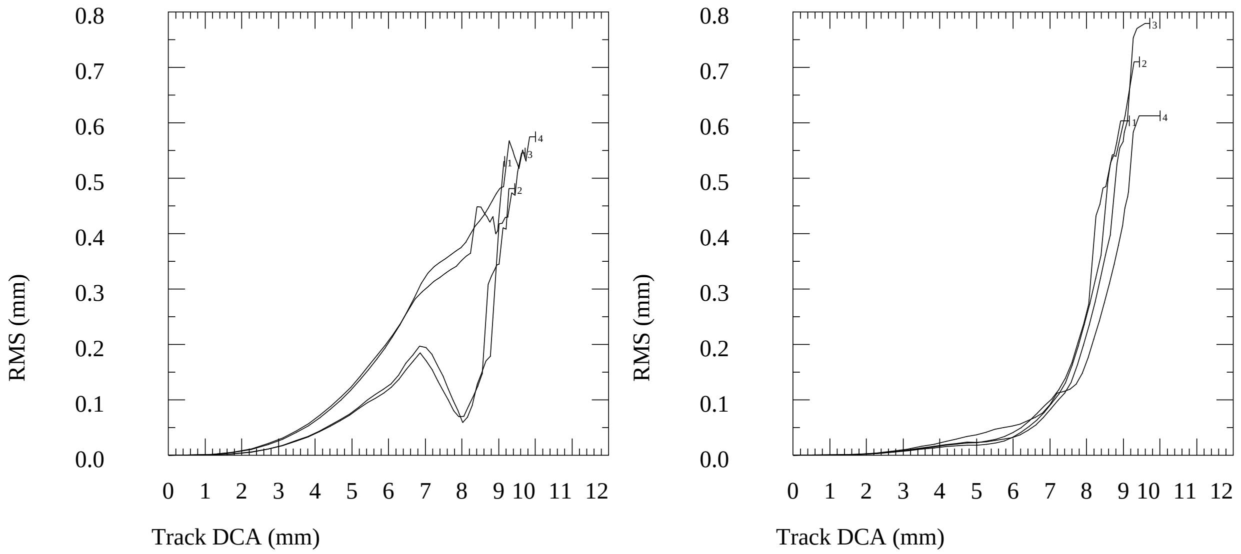

Figure 5-11. *Distortions in a rectangular cell vs. the track's distance of closest approach. The distortions are calculated over a range of track angles with a single time-distance relationship. The four curves show distortions in the four layers in a superlayer in the axial-stereo design, for tracks which are within $\pm 30°$ of the radial direction (i.e., $p_{\mathrm{t}} > 350$ MeV/c in an 80 cm drift chamber). The left plots are for the case with all field wires at ground voltage, while the right plot has +230 V on the cell corners along the enclosing layers and −120 V on each pair of field wires between the sense wires.*

Cell Geometry	Cell Size dr × dz (mm × mm)	Distortion % of cell (see text)	Performance % of cell (see text)
Rectangular 6:1	15.0 × 20.2	78.	73.
Square 5:1	15.0 × 15.4	86.	71.
Square 4:1	15.0 × 15.4	76.	69.
Hexagonal 5:1	15.0 × 20.2	80.	74.

Table 5-5. *Time-distance distortions and resolution performance of cells. The distortion column gives the percentage of the cell width that has less than 100 μm of rms variation in the time-distance relationship. The performance column gives the percentage of the cell width that produces signals with at least two primary electrons collected within the first 10 ns of the pulse shape. These values are for tracks within $\pm 30°$ of the radial direction in an 80:20 He:C_4H_{10} gas mixture and a 1.5 T magnetic field.*

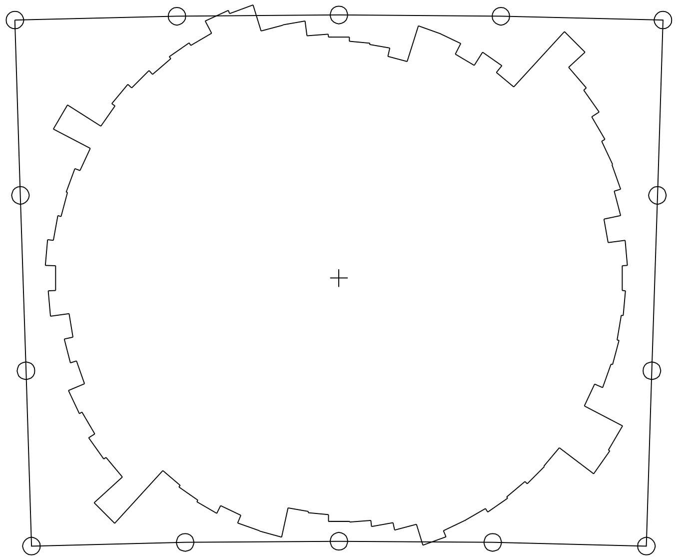

Figure 5-12. *Spatial resolution performance in a rectangular cell, as described in the text. The jagged contour depicts track angles and impact parameters at which an average of at least two primary clusters will contribute to the first 10 ns of the pulse shape.*

has been calculated at each track angle for regions which satisfy this criterion. Tracks with larger DCA values generally have shorter collection regions within the 10 ns window, and therefore poorer resolutions, while tracks with smaller DCA values have better resolutions. A contour plot of these DCA performance limits as a function of the track angle is shown in Figure 5-12 for rectangular cells. The ratio of the area within the contour and the geometric area of the cell is a figure of merit for the cell. Table 5-5 shows these values for various cell geometries with the number of field wires per sense wire shown (6:1). The 5:1 square cell has the least distortion. The rectangular and hexagonal cells are somewhat worse. The square cell (4:1 field wire to sense wire ratio), having only one field wire between sense wires, has the most distortion.

5.4.5 Gain Variations

Gain variation as a function of z position has been studied using DCSIM, which computes charge densities on sense wires. The gain changes within cells are based on the approximate relation that a 1% change in the charge on the wire results in a 20% change in avalanche gain. In the axial-stereo design, the charge on the wire varies due to the varying cell widths within superlayers and the varying radial size between enclosing layers at boundary cells. The largest gain variation of boundary cells is found to be $\pm 3\%$, while the largest gain variation between an inner layer and an outer layer in a superlayer is $\pm 4\%$. In the all-stereo case, the $\pm 3\%$ increase in cell width at the ends of the wire length leads to a gain variation of less than $\pm 2\%$ along the wire length. Gain changes due to field wires' phase locations relative to the sense wires from cell to cell in a layer are miniscule in the all-stereo case.

5.4.6 Electrostatic Forces and Stability

Electrostatic forces and stability limits have been simulated using DCSIM. The accuracy of the program has been verified with observed wire deflections in the 100-wire test chamber, Prototype I. For this purpose, the 2.5 m-long sense and field wires were tensioned with only 9 g so that wire instability could be observed at nominal high voltage. For the *BaBar* chamber, at the nominal stringing tension, the predicted deflection due to electrostatic forces is 160 μm for the worst case wire, and the instability point is far from the operating point. Therefore, for the present cell configuration, it appears that there is no problem with electrostatic deflections or stability.

5.4.7 Pattern Recognition Studies

Axial-Stereo Case

In similar chambers in other detectors, pattern recognition is performed by finding track segments within each superlayer, and then linking segments to form tracks. The left-right ambiguity resolution is done during the segment finding. The axial segments are linked to form circles in the x-y plane, while the stereo segments provide the z and θ coordinates. After segments have been linked, a full three-dimensional fit is made to all the wire hits. Part of this pattern finding and fitting has been done for the prototype chamber. Some losses may arise at lower momentum due to the reduced efficiency for segment finding within a superlayer or difficulties in segment linking for tracks with significant curvature, particularly for those particles which do not originate from the interaction point.

All-Stereo Case

Several studies concerning pattern recognition and track reconstruction in an alternating-layer all-stereo chamber have been made in order to investigate potential limitations of having only two views. In particular, two independent approaches to the pattern recognition problem have achieved efficiencies between 95% and 99% (depending on method and backgrounds) for finding tracks despite the noncircular projections in the stereo views. The absence of superlayers also raises a concern about unresolvable left-right ambiguities in a single view. This has been shown to occur for less than 0.5% of tracks from generic $\Upsilon(4S)$ events, and appears to be further reduced by a factor of 2 by the careful choice of the azimuthal offsets of each layer. Most of the ambiguities that do occur are expected to be resolved by information from the other view. Finally, the possible mismatching of track projections found in the two views has been investigated using a parameterized approach [Bri93] and with full pattern recognition and fitting. Both studies indicate that genuine mispairing of projections from opposite views happens in about 0.5% of all cases. With extreme backgrounds, and depending on the matching criteria, mismatches for up to 2.8% of tracks have been found. Most of these, however, arise from the inclusion of small segments of an additional track, or fake track, in one view; the actual contribution to track-finding inefficiency is estimated to be less than 1%.

5.5 Gas Choice and Properties

The choice of gas for the drift chamber is driven primarily by the needs to reduce the total amount of material, minimize multiple scattering for low momentum tracks, and to operate efficiently in a 1.5 T magnetic field. These requirements are quite well satisfied by mixtures of helium and hydrocarbons. In particular, mixtures with 10–30% of various hydrocarbons afford a small Lorentz angle, good resolution, and low multiple scattering. In Table 5-6, the properties of the baseline gas choices are shown, along with other possibilities which have been considered for use in the *BaBar* Drift Chamber. The drift velocities and Lorentz angles are determined with the Boltzmann integration code MAGBOLTZ [Bia89]. The *dE/dx* calculations are performed with a modified version of a program from Va'vra *et al.* [Vav82]. The table shows that the helium mixtures under consideration have a radiation length more than five times larger than that of HRS gas, $Ar:CO_2:CH_4$ 89:10:1, a commonly used argon-based mixture. Figure 5-13 shows the calculated drift velocity *vs.* electric field for four of the gases in the table. The helium-based gases are not saturated, but lead to better performance than typical argon mixtures, since the smaller Lorentz angle results in a more uniform distance-time relationship.

The two gases which have received the most attention are an 83:10:7 mixture of $He:CO_2:C_4H_{10}$ and an 80:20 mixture of $He:C_4H_{10}$. These gases and the benchmark argon mixture, HRS gas, have been studied in a prototype chamber, which is described in Section 5.11. The results for the spatial resolution obtained in these studies are summarized in Figure 5-14. Both helium-based gases provide good spatial resolution. The 80:20 $He:C_4H_{10}$ mixture is our preference based on measured spatial resolution and simulated *dE/dx* resolution, although there are concerns regarding the safety implications if this proves to be a flammable gas. We have also studied whether these gases exhibit gain changes or high-voltage breakdown

Gas Mixture	Ratio	X_0 (m)	Primary Ions/cm	v_d (μm/ns)	θ_L (deg)	dE/dx Resol. (%)	K/π Separation p for 3σ (MeV/c)	# of σ at 2.6 GeV/c
$Ar:CO_2:CH_4$	89:10:1	124	23.6	49	52	7.3	665	2.4
$He:C_2H_6$	50:50	686	23.1	31	45	6.6	720	2.1
He:DME	70:30	723	22.4	6	8	6.7	720	2.1
$He:C_3H_8$	70:30	733	24.1	24	36	6.5	730	2.2
$He:C_4H_{10}$	80:20	807	21.2	22	32	6.9	710	2.1
$He:CO_2:C_4H_{10}$	83:10:7	963	13.8	19	26	8.5	660	1.7

Table 5-6. *Properties of various gas mixtures at atmospheric pressure and 20°C. The drift velocity (v_d) and Lorentz angle (θ_L) are given for an electric field of 600 V/cm with no magnetic field and with 1.5 T, respectively. The dE/dx resolution is calculated for a minimum-ionizing particle. Also listed are the momenta below which there is at least 3σ K/π separation, and the K/π separation at 2.6 GeV/c.*

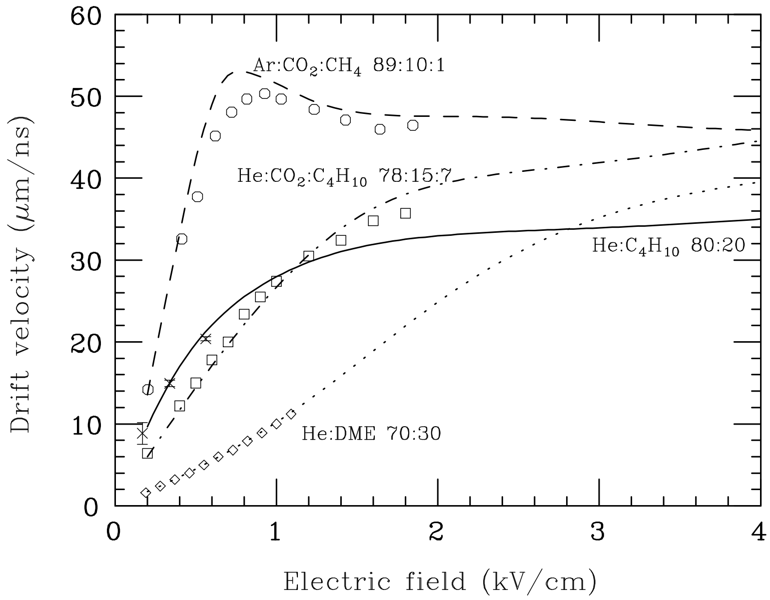

Figure 5-13. *Calculated and measured drift velocities as a function of electric field for zero magnetic field. The calculations use the code of Biagi (see text). The solid curve and crosses* [Pla92] *are for the 80:20* $He:C_4H_{10}$ *mixture; dot-dashed curve and squares* [Boy92] *are for 78:15:7* $He:CO_2:C_4H_{10}$*; the dotted curve and diamonds* [Cin91] *are for 70:30* He:DME*; and the dashed curve and circles* [Boy92] *are for (89:10:1)* $Ar:CO_2:CH_4$ *(HRS gas).*

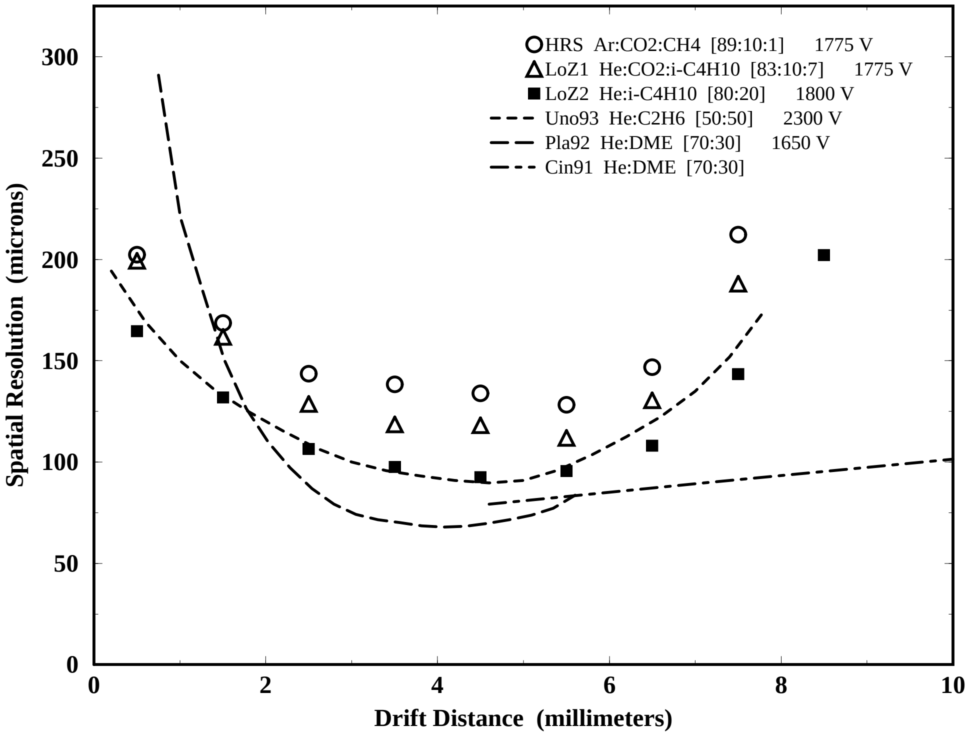

Figure 5-14. *The prototype drift chamber results for* HRS *gas,* He:CO_2:C_4H_{10}, *and 80:20* He:C_4H_{10}. *Points represent data from the Prototype I chamber; curves are the results of studies performed elsewhere.*

after a period of irradiation. The aging studies were performed with a small proportional counter and an ^{55}Fe source. All of the helium-based gases in Table 5-6 were tested except for the DME mixture. The isobutane and propane mixtures showed negligible aging. The 50:50 He:C_2H_6 and 78:15:7 He:CO_2:C_4H_{10} mixtures both had some gain loss, equivalent to $\sim$30% for an accumulated charge of 1 C/cm. These studies indicate that all of these gases are appropriate for our purposes since the expected charge accumulation over the lifetime of *BaBar* should be under 0.1 C/cm. Further long-term aging studies are planned.

Angle (Degrees) Outer/Inner	Thickness (mm)	Deflection (mm)	Maximum Stress (MPa)
0/20	6.5	36.2	154
5/20	6.5	18.3	75
10/20	6.5	6.6	50
20/20	6.5	2.2	32
30/20	6.5	1.2	24
20/20	4.7	3.4	51

Table 5-7. *Finite-element calculations of deflections and stress for various endplate shapes. A 2400 kg load was evenly applied between 22.5 and 80 cm and supported at the outer radius. The endplate is supported at the outer radius only, and the maximum deflection occurs at the inner radius.*

5.6 Mechanical Design

5.6.1 Endplates

The chamber endplates must support the wire load of ~2400 kg yet be of negligible thickness in radiation lengths to minimize photon conversion before the calorimeter. The offset of the chamber and the beam energy asymmetry at PEP-II lead to boosted events such that photons with $\cos\theta_{cm} > 0.67$ exit through the forward endplate, while only those with $\cos\theta_{cm} < -0.91$ exit through the rear endplate. The two endplates will be identical, but the readout and high-voltage connections will be installed on the backward endplate only.

The choice of carbon fiber as the structural material and the application of the double cone geometry shown in Figure 5-2 allow for extremely thin endplates. The material proposed is an intermediate modulus graphite fiber IM7 [IM7] coupled with a toughened epoxy (977-2) or a cyanate ester resin system (954-2). The mechanical advantage of the double-cone shape is illustrated in Table 5-7 which shows material thicknesses, deflections under wire load, and maximum stress for various endplate configurations. The entries in the angle column represent the angles of the outer and inner cones with respect to a flat endplate—thus 0/0 would be a flat end plate, and 20/20 is closest to the 22.7° symmetric cone illustrated in Figure 5-2 as the baseline design. The scale for acceptable deflections is set by the 9 mm elongation of the aluminum field wires under the 53 g stringing tension. The factored limit stress in carbon fiber is estimated at 61 MPa, which includes a de-rating factor of 3 for the holes, and a safety factor of 3.

The double-conical endplate provides substantial mechanical advantages without seriously degrading the forward tracking length, or introducing too large an angle for axial drilling of the feedthrough holes. The radius of curvature at the cone tip (the transition between the inner and outer cone) has been limited to 50 mm in order to reduce the stress associated with sharper angles. The curvature also allows better laminate properties in the transition area by reducing fiber breakage due to expansion and contraction during the cure and allows the hole pattern to be drilled without any discontinuity.

The endplate thickness of 6.5 mm corresponds to 2.8% of a radiation length; the feedthroughs (1.2%), rf-shield (0.6%), and cable support spider (0.4%) roughly double the material thickness of the forward endplate to about $0.065X_0$. Cables, preamplifiers, and HV boards add an additional $\sim 0.1X_0$ to the backward endplate. The endplates will be laid-up on a mandrel, covered with rubber cure pads, then bagged and cured in an autoclave. Both of the resin systems under consideration are cured at 350°F under a pressure of 100 psi. A 3 mm sacrificial layer of nonstructural material will be applied to the outsides of the endplates. A considerable fraction of this layer is then removed as flat annuli are machined for each wire layer as shown in Figure 5-15. These surfaces allow machining tools to make a perpendicular approach to the surface when drilling the feedthrough holes and provide a registration surface for the feedthroughs.

The holes for the field wire feedthroughs will be approximately 2.5 mm in diameter, while the sense wire holes will be 5–7 mm in diameter, depending on the choice of restringing options currently under consideration. The holes will be drilled axially, which simplifies the drilling process, the hole survey, and connections to the electro-mechanical boards. The wires exit from the feedthroughs at the appropriate stereo angle, and the wire position accuracy is therefore weakly coupled to the insertion depth of the feedthrough. The depth of insertion is controlled by the machined annuli, which act as registration surfaces.

5.6.2 Inner Wall

For good p_{t} resolution, it is essential to minimize the material between the silicon vertex detector and the drift chamber. The inner wall of the chamber lies immediately outside the $0.005X_0$ support tube and represents a small amount of material by comparison. The inner wall is not required to carry any of the wire load but must support any differential pressure between the inside and outside of the chamber.

An engineering case study has been performed [Smi94], which assumed that the inner wall must withstand a test pressure of 2 kPa (20 mbar), and the results are summarized in Table 5-8. While beryllium would provide a minimal amount of material, this option would be very expensive and unlikely to be feasible with the required thickness of less than 0.5 mm. Therefore, the inner wall will be constructed from 0.4 mm of the same carbon fiber

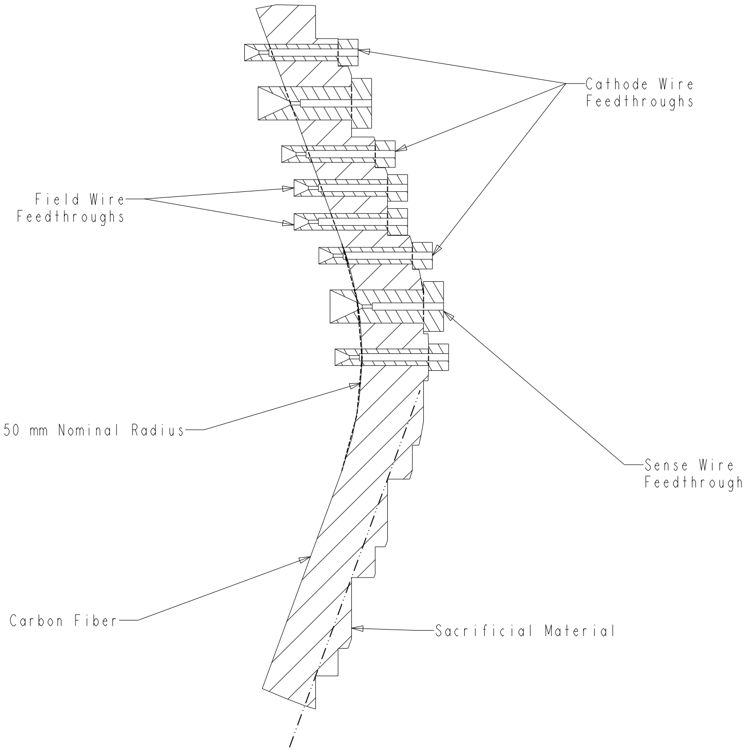

Figure 5-15. *Cross section through the endplate cone tip showing the feedthrough seating. Narrow annuli are milled to seat feedthroughs in the cathode layers and alternate with wider annuli containing the sense wire feedthroughs and, in the case of a 6:1 cell design, pairs of field shaping wires.*

as the rest of the chamber. An rf-shield will be required which will contribute an additional 0.1% of a radiation length, and concerns about helium permeability may lead to a Mylar layer as a gas seal.

5.6.3 Outer Wall

The outer wall bears the axial wire load between the endplates. The large circumference allows this load to be supported by as little as a 1.6 mm-thick ($0.006X_0$) carbon-fiber tube. In order to be robust against local impacts, a 3.2 mm-thick ($0.012X_0$) option is being pursued as more realistic. This is still a small amount of material in comparison to the $0.18X_0$

Material	Thickness (mm)	% of Radiation Length
Radel [RAD]	2.45	0.82
Vitrex PEEK 450G [VIT]	2.19	0.73
Carbon Fiber IM7/977-2 [IM7]	0.40	0.15
Beryllium	0.32	0.09

Table 5-8. *Inner wall thickness required to withstand a test differential pressure of 20 mbar, determined from Roark's Formulae [You89] assuming no stiffeners and ends held circular.*

contributed by the DIRC, which is located between the outer wall of the tracking chamber and the calorimeter.

During operation, the chamber will be maintained at a constant temperature. However, during transport, downtime, and other anomalous situations such as magnet quenches, relatively large temperature fluctuations might be encountered; in such cases, thermal expansion can lead to significant changes in wire tension. An aluminum outer wall would provide a perfect thermal match to aluminum field wires but lead to an increase in the tungsten sense wires' tension of about 0.5% per °C. The thermal expansion coefficient of carbon fiber is well matched to that of the sense wires but leads to a decrease in the aluminum field wire tension of 0.8% per °C. The sign of this effect and the fact that the field wires rather than the sense wires are at risk make carbon fiber preferable to an aluminum shell.

The outer tube will be constructed of the same material as the endplates. An aluminum foil will be adhesively bonded to the outer surfaces to provide rf-shielding. The inner surface may be treated with a carbon spray to ensure adequate electrical conduction to drain charge. The low moisture absorption characteristic of the carbon fiber is expected to eliminate any concerns about humidity control.

5.6.4 Joints

The inner and outer walls will be installed after the chamber wires have been strung. The outer joint is within the physics acceptance, so every effort must be made to minimize the amount of material. Both joints must occupy minimal radial space to preserve the maximum possible tracking length. The outer wall will be attached using a double-labyrinth gluing technique that has been used on several previous chambers. A conceptual sketch of the outer joint is shown in Figure 5-16. For gluing, the chamber is turned vertically and epoxy is injected via many syringes into the lower labyrinth and eventually flows to the upper.

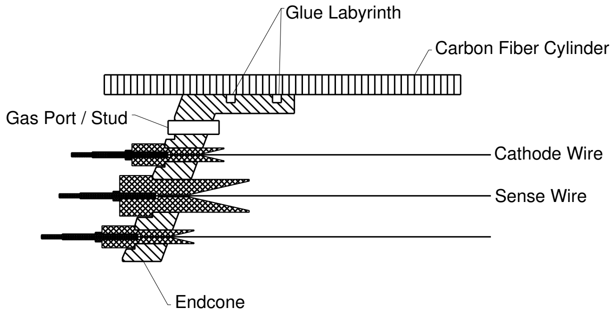

Figure 5-16. *Conceptual design for the outer-wall/endplate joint.*

The glue injection ceases once the upper recess is filled and glue starts to appear at small air-escape holes.

The inner joint is not within the acceptance region of the detector, so the amount of material is not critical. A removable joint, using an O-ring gas seal, will be used. If at some future date the support tube were removed, this would allow the option of replacing the inner wall with a lower-mass alternative.

The inner and outer joint regions must also accommodate gas fittings and attachment points, the latter being used both for supporting the chamber and for pretensioning the endplates prior to stringing. A ring of studs will be embedded in the carbon fiber endplates at the outer and inner radii during the fabrication process. The studs alternate in an appropriate ratio with gas fittings. The advantage of embedding during fabrication is that none of the structural fibers are broken.

5.6.5 R&D Program on Structural Components

The proposal to use carbon-fiber laminates as the main structural component of the chamber requires a thorough research and development program. Such materials are widely used for applications such as satellite structures [Bra94], in which extreme physical conditions are coupled with zero access for maintenance. For high-energy physics applications, the long radiation length of carbon fiber (about 25 cm) is an additional attraction. The R&D program will examine basic material properties and fabrication techniques using small samples, or coupons, followed by the evaluation of increasingly substantial engineering models which address specific areas of concern, leading eventually to the construction of a full-sized prototype endplate. In parallel with this process, theoretical models will be developed to allow the calculation of properties using finite element analysis and classical lamination theory. The interaction between these parallel developments should lead to a complete mechanical specification and an integrated finite element analysis model of the entire chamber prior to the construction of the full-sized prototype.

At the coupon level, investigations will include evaluation of basic material properties with standard tests (American Standard Test Methods) such as tensile strength (ASTM D3039), humidity absorption (ASTM D560), and adhesive tensile lap strength (ASTM D1002). Design-specific tests such as the evaluation of outgassing effects on chamber aging and the helium permeability of the proposed laminates will be performed. Extensive drilling tests can also be carried out at this stage in order to investigate hole accuracy, ovality, breakout, tool-bit wear, lubricant absorption, procedure elapsed time, and quality assurance techniques.

Engineering models will be developed to address the joint design with respect to strength, gas-seal, and assembly procedure. Model tubes will be constructed to verify compression and buckling calculations. The insertion, seating, and gas-seal of the feedthroughs will be investigated, and a full segment of the endplate will be constructed to confirm the laminate lay-up and cure procedures.

After the engineering model tests and the laminate design have been completed, and after a manufacturing technique, a machining strategy, and quality assurance methods have been developed, a full-sized prototype endplate will be constructed and partially drilled to verify the entire fabrication procedure. Such a prototype may subsequently be further drilled to investigate deflection properties and could be shipped to the stringing site for evaluation of the proposed prestressing and load transfer technique.

5.6.6 Wires

Transverse momentum resolution is dominated by multiple scattering up to the highest momenta of interest. This has led to the design of a chamber with low-mass field wires and a helium-based gas. Aluminum has a relatively long radiation length and is a good field wire candidate. Bare aluminum is not suitable, however, because oxidation forms an insulating layer on the wire surface leading eventually to electrical discharges. Previous chambers have used gold-coated aluminum, but thin uniform layers of gold have been hard to achieve. We plan to use 55 μm-diameter aluminum wire with a 0.50 μm gold coating. The contribution of the gold to the total radiation length is roughly equal to that of the aluminum. Unfortunately, gold coatings this thin tend to flake off and provide nonuniform coverage. Other alternatives, such as silicon carbide wires and nickel-coated aluminum wires, have been investigated but proved unacceptable.

Aluminum wires also suffer creep, causing wires to lose tension over time. With careful choice of the wire type, this can be limited to an acceptable level of less than 0.1% of the wire length per year after an initial rapid increase in length over the first few hundred hours.

The relative softness of aluminum means that considerable care must be taken to design a reliable crimping procedure.

For the sense wires, 20 μm tungsten is proposed, which would contribute approximately one-half the material contained in gold-plated aluminum field wires. Although tungsten-rhenium has recently become popular as a wire material, its use has been ruled out for the *BaBar* drift chamber due to the ~50% increase in resistance, which would degrade the signal-to-noise performance of the chamber. Some consideration is being given to a larger 30 μm wire to improve signal preservation of signal amplitude from the forward end of the chamber. This would increase the sense wire material by a factor of 2.25, making it comparable to the field wires.

Wire aging and cross-talk tests will be performed, and a full understanding of the mechanical and electrical wire/feedthrough/endplate interface will be sought using a full-length prototype chamber, Prototype II.

5.6.7 Feedthroughs

Feedthroughs insulate field and sense wires electrically from the endplates and provide for accurate wire placing. They must be inexpensive to manufacture, must provide a gas seal, and must not react chemically with the chamber gas.

A preliminary field-wire feedthrough design is shown in Figure 5-17. The body of the feedthrough is a single piece of injection-molded plastic with a 2.5 mm precision outer diameter and a length of about 15 mm. Wire positioning is provided by a separate brass insert containing a 100 μm-diameter precision hole. This has a 1 mm bend radius on the feedthrough exit end to avoid kinking stereo wires. A metal insert (brass) was chosen to provide low electric field density at the interface with the plastic body, avoiding discharge problems in the insulator. Delrin or celenex plastic insulation is presently being considered.

The wire is secured in the feedthrough using a gold-plated aluminum crimp pin of a design similar to that used successfully in several TRIUMF-built drift chambers. The TRIUMF pins were actually made of brass, which has the advantage of providing a more rigid contact for connecting the electro-mechanical boards, but provides for a narrower tolerance for crimping wires than a softer material such as aluminum. Good results in terms of wire breakage have been obtained at SLD where aluminum wires were crimped in softer aluminum crimp pins. The small diameter region of the crimp pin is the crimp locator, while the large diameter region is used for electrical connections. This separate-function design is expected to reduce a crimp-pin breakage problem observed at SLD, where the mechanical connections were made in the same region as the crimp.

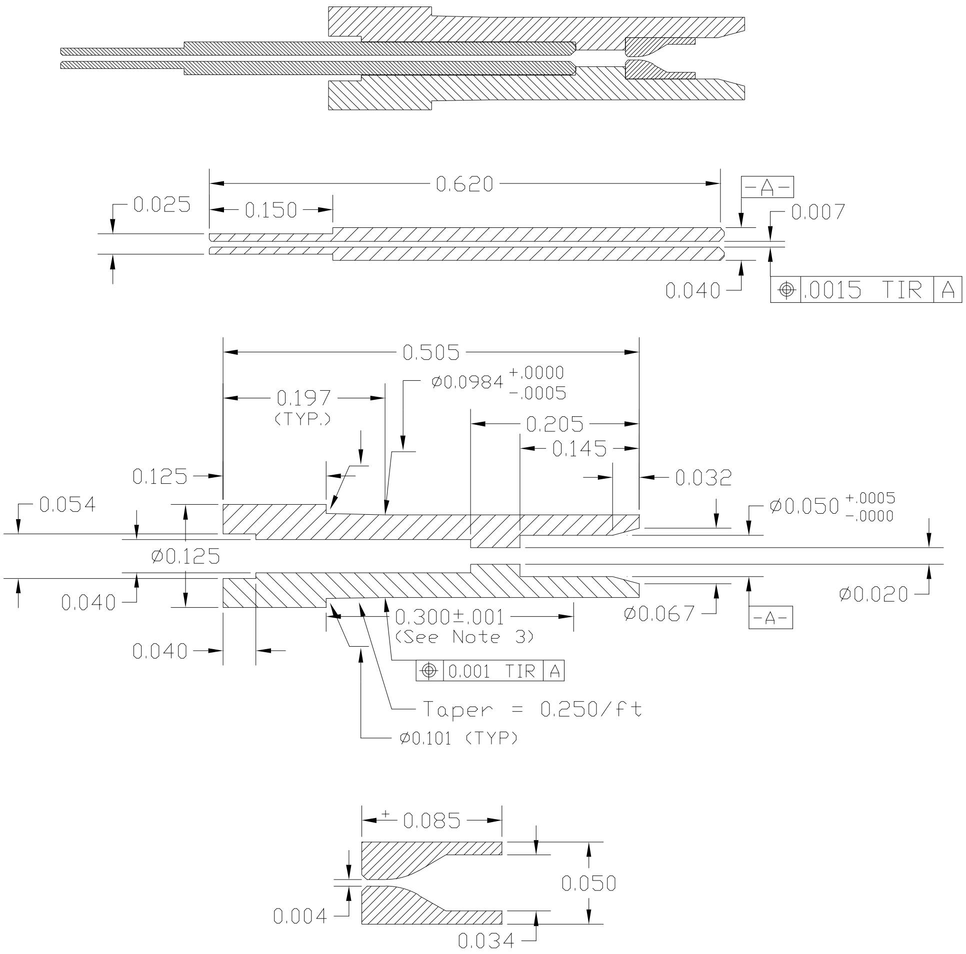

Figure 5-17. *Field-wire feedthrough design, showing crimp pin, Delrin sleeve and precision brass insert for wire location.*

Wire positioning is provided by accurate centering of the 100 μm locator hole in the brass insert of the feedthrough. Measurements of 1000 feedthroughs manufactured using a similar design for the Beijing Energy Spectrometer (BES) showed that the concentricity of the precision hole with respect to the feedthrough outer diameter was 11 μm. The feedthrough itself is required to have an outer-diameter tolerance of 10 μm, as was achieved with the BES feedthroughs, and must be fitted tightly in the endplate hole.

The gas seal is provided by a slight (1:48) taper at the back of the feedthrough, which may be adjusted to provide the desired degree of press fit into the endplate. The crimp pin is press fit in the plastic body and may be sealed with epoxy if necessary.

The sense-wire feedthrough design will have a larger (5–7 mm) outer diameter and a longer body (25 mm). This provides both thicker insulating walls and a longer projection from the endplates to better shield the HV from the grounded endplate. The precision inserts will be identical to those used for the field wires, and a brass/copper crimp will be used.

Feedthrough prototypes are expected to be available in early 1995. Planned tests include dimensional tolerance checks both at the time of molding and over long term to study stability, as well as checks of the electrical properties of the feedthroughs. The Prototype II chamber will use the new feedthroughs to test their performance in a real chamber environment, including electrical isolation and gas leakage tests.

5.6.8 Stringing

The chamber will likely be strung in a large clean-room at TRIUMF in Vancouver. The 7.82×11.45 m, Class 10,000 clean-room has a ceiling structure containing lighting fixtures and 18 distributed HEPA-filter/air intake blowers. The stringing stand proposed for the chamber would be about 2.0×4.7 m and would require a ceiling height of about 6.0 m when rotated into the vertical position. This would necessitate raising the ceiling of the TRIUMF clean room by about 3.0 m. Temperature control ($\pm 2^{\circ}$C) will also be installed.

The chamber will be strung horizontally without the outer or inner cylindrical shells in place. Each endplate will be attached from its outer edge to a central axle of the stringing stand by means of external support spiders. The endplates will be preloaded at their inner radii, and possibly at intermediate positions as well. All loads are transferred to the central axle by the spiders. Stringers will be able to work between and under this support structure, while the interior region of the chamber is completely unobstructed.

Two teams of three people (or two people and a robot) each may work simultaneously as the chamber is strung from the inner radius out. The wire is inserted through one endplate by a stringer, transported to the other endplate either by the robot or by the third stringer, and is then inserted though the appropriate hole for the second stringer. Both stringers thread the wire onto a feedthrough/crimp-pin assembly and insert the assembly into the endplates. When the first stringer has crimped one end of the wire, the second stringer may tension and crimp the other. A robot would offer a smooth method of transporting the wire and would ensure that the correct hole was used. Depth perception is notoriously bad when looking at a field of strung wires, and a robot would help to avoid stringing errors. The chamber can also be kept cleaner by enclosing the space between the endplates, including the robots, in a very clean tent within the outer clean room.

Wires which fail during the stringing process will be restrung with the chamber rotated into a vertical position, aligned at the appropriate stereo angle. A magnetized needle will be

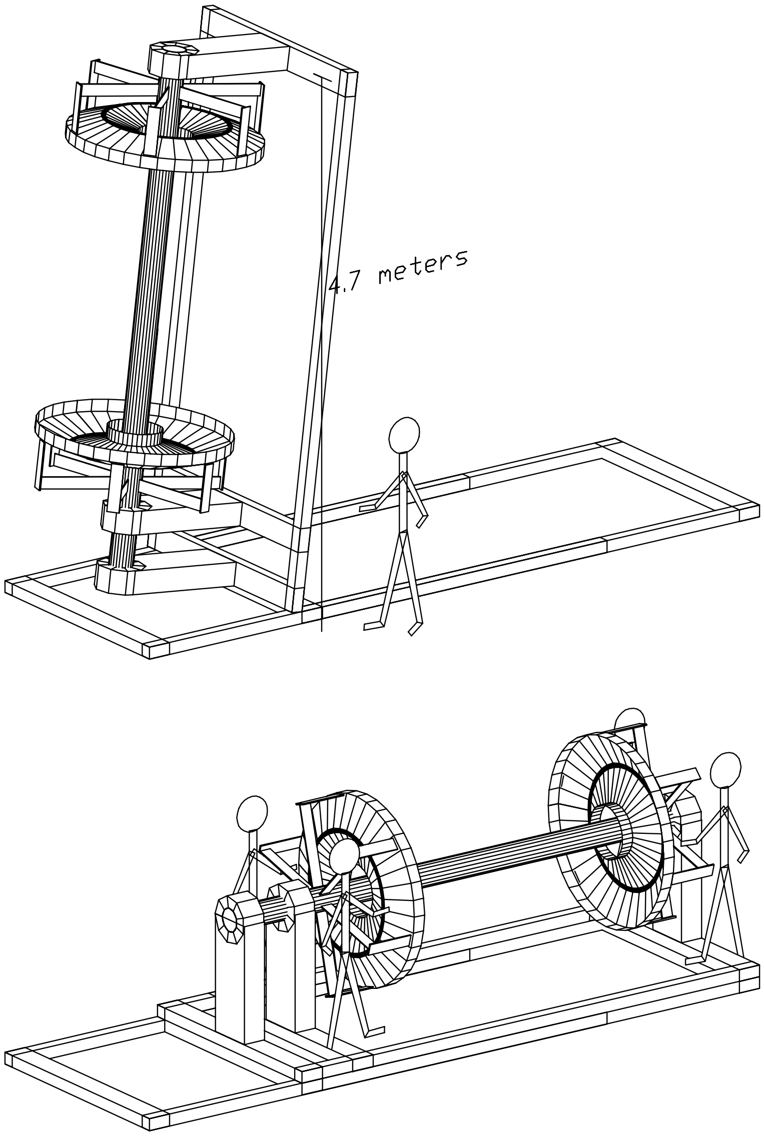

Figure 5-18. *The stringing and pretensioning stand for chamber assembly, showing the normal horizontal position for wire insertion with two stringing teams and a vertical position for wire replacement.*

lowered through the top hole and captured by a similar needle inserted into the lower hole. The stringing stand illustrated in Figure 5-18 has a dual support at one end, allowing the chamber to be cantilevered for the installation of the inner and outer shells. The inner wall supports no axial load and is installed after stringing to avoid accumulation of dust.

5.6.9 Endplate Connections

Electro-Mechanical Boards

The electro-mechanical boards form the interface between the feedthroughs and the electronics. They perform the following functions:

- Provide a ground plane for the cathode wires at both ends of the chamber. Insulating feedthroughs are being used for the field wires to allow tension measurements to be performed and broken wires to be located. In the axial-stereo layout, some of the cathode wires will be biased at a few hundred volts, which also requires insulated feedthroughs.
- Provide high voltage to the sense wires. This will be done on the backward endplate only.
- Provide collection of signals from sense wires and distribution of calibration pulses to a standard preamplifier card. All signals will be extracted from the backward endplate. No cables will be present on the forward endplate.

Thin cathode boards are mounted on both ends of the chamber and separate sense wire boards are mounted on the backward endplate only. The cathode boards are copper-coated, printed circuit boards approximately 0.25 mm thick, providing a low-resistance, low-inductance connection. A good quality ground is essential to avoid cross-talk between sense wires arising from induced transient signals on neighboring field wires (Figure 5-19). The boards are mounted parallel to the endplate and connect to the cathode wire feedthrough pins. Each cathode board is connected to neighboring boards with removable jumpers for the ground and bias voltages.

The $\sim$0.25 mm-thick sense-wire circuit board is mounted on the backward endplate parallel to the cathode boards but separated by approximately 6 mm to avoid high voltage (HV) breakdown. The connection to the sense-wire crimp pins is made through the large holes in the cathode boards as illustrated in in Figure 5-19. At the forward endplate, the sense-wire crimp pins will be capped to prevent corona discharges into the air. The sense wire boards will provide a standard connection for the preamplifier cards, for ease and safety of

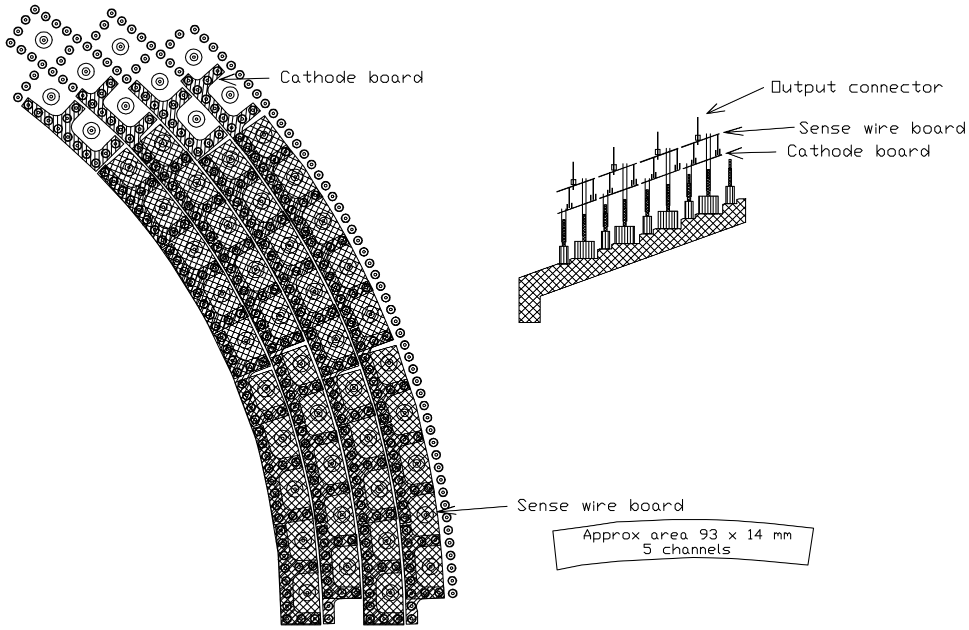

Figure 5-19. *One concept for endplate cathode boards for grounding field wires and HV/signal distribution boards. In this example, the cathode boards connect together 12 cathode wires and are jumpered together to form the ground plane. The sense wire boards mount over the ground plane and provide a standardized connection between the preamplifiers and five sense wires.*

installation and replacement. The cathode boards and sense wire boards will rarely, if ever, be removed.

The sense wire boards will also include a HV bus, as well as the isolating resistors and capacitors that couple to the sense wires. Jumpers will connect adjacent boards in the ϕ-direction, allowing distribution of high voltage. This scheme allows the HV to be applied without the preamplifier cards attached, which offers greater flexibility and safety during testing or troubleshooting.

Preamplifier Cooling

At a constant voltage, the gas gain depends strongly on the gas density, which is proportional to pressure and inversely proportional to temperature. Therefore, for good dE/dx resolution, both the pressure and temperature must be kept constant or at least be well-monitored. While pressure is always uniform across the chamber, temperature differences at the chamber surface may generate differences within the gas volume. The total heat generated by the preamplifiers is on the order of 35 W and may be removed by flowing nitrogen gas.

Cables

The coaxial HV cables and ribbon-style signal cables will be attached to the backward endplate only. A typical HV cable as considered here has a 3 mm outer diameter and corresponds to about 6% of a radiation length. Approximately 220 cables will be routed radially over the endplates to the various HV distribution points. The volume of HV cables is sufficiently small that only a single layer will be formed at the outer radius of the chamber.

The ribbon cables supply the preamplifiers with power, carry test lines, and the preamplifier outputs. A typical unshielded PVC coated ribbon cable is 33 mm wide, 2 mm thick, and corresponds to 0.75% of a radiation length. The cables are stacked six deep, corresponding to 4.5% of a radiation length at the outer radius.

A low-mass structure is required to support the cables over the endplate. The anchor points will be the studs at the inner and outer wall joints. Cables are supported on a spider-like structure which will be constructed of three rings, one each at the inner radius, the cone tip and the outer radius, connected by spokes. In the axial-stereo case, intermediate connections to the endplate are possible at the three hole-free superlayer transition regions. Approximately 6 cm of clearance is required between the endplate and the support to allow for card replacement.

5.7 Front-End Electronics

The front-end electronics provide amplification and shaping of the signals for optimal timing and pulse height (dE/dx) resolution. We have identified parameters of the drift chamber which will impact the design of the front-end electronics. For example, the combination of wire resistance and terminating resistor is being optimized for best signal/noise behavior. The shaping time and required dynamic range depend on the drift gas selected and the mode of drift time measurement (TDC, FADC) and are the subject of simulations. In order to optimize power and noise performance, the on-chamber, front-end electronics will consist of a bipolar ASIC chip serving several channels. The front-end electronics are mounted on PC boards, which connect directly to the feedthrough pins on the backward endplate.

The amplified signals are transmitted about 30 m to the readout cards using shielded twisted pairs. The signals are differential to minimize the emission of electromagnetic interference and to allow for common mode rejection at the ends of the transmission lines. They are sent to a readout card containing discriminators and pulse-height digitizers based on a deadtimeless FADC system. The discriminator outputs are used by the trigger segment finder logic, and the FADC samples are stored continuously in a buffer memory. When a trigger is received, the FADC samples are read from the dual port buffer memory, and the drift time and charge information is extracted from the FADC raw data and transmitted to the event builder. The sampling clock will probably run at 79 MHz, a submultiple of the 238 MHz machine frequency. This will allow the suppression of recurrent machine-related noise and yield a timing resolution on the order of 2 ns, which is sufficient to match the intrinsic position resolution of the chamber (about 125 μm). Further details of this readout system can be found in Chapter 10.

5.8 High Voltage System

The high voltage (HV) system will provide $\sim$2 kV to the 7000 sense wires while minimizing the impact of HV problems, such as sparking in the chamber, broken wires, and failed HV capacitors. Forty HV supplies will be used to drive approximately 220 HV cables. This number ensures that a very low current is drawn even with high background levels. A sensitive trip level will protect against wire breakage due to sparking. Forty supplies will also provide enough current to ramp the HV in less than ten seconds, thereby minimizing detector downtime during frequent injections. A possible implementation would involve using the LeCroy 1454 system, consisting of a mainframe interfaced to VME or CAMAC which houses four HV cards, each having 12 channels capable of providing up to 3 kV and 2.5 mA.

In the example illustrated in Figure 5-19, a set of five sense wires receives voltage from a single HV-distribution card located on the backward endplate. The HV card contains a HV bus with jumpers to adjacent cards, and an isolation resistor and one or two decoupling capacitors for each wire. The resistor values for the sense wires will be approximately 0.5MΩ per wire, ensuring that the voltage drop across the resistor is $\leq$ 1 V. The induced current in the first sense-wire layer has been estimated to be approximately 50 nA for the nominal background levels. Two HV capacitors mounted in series would mean that a single failure (short) would not affect the performance of the chamber; however, space limitations on the endplate may not allow this solution. The capacitance value will be selected on the basis of signal propagation measurements and calculations.

Each HV cable supplies four such HV distribution cards; the jumpers are used to distribute the voltage between cards. If there is a HV problem, 32 sense wires ($\sim$0.3% of the total) will be affected until the next access to the drift chamber endplate.

5.9 Calibration and Monitoring

5.9.1 Calibration

The timing characteristics and the gain of the electronics chain will be calibrated with a pulser system. The input of every preamplifier channel is connected via a coupling capacitor and isolating resistor to a calibration bus. When a voltage step is applied to the bus, a defined charge is injected into the front-end of the preamplifier, and the whole electronics chain can be calibrated. The matching of these calibration capacitors on bipolar ASICs is excellent. It has been shown to be advantageous to connect neighboring channels to different calibration buses. It is planned that every chip will be serviced by four buses, and that these buses will be distributed to a limited area of the drift chamber, similar to the case of the high voltage and preamplifier power supplies.

5.9.2 Slow Controls

The slow control system will monitor the operation of the drift chamber, the high voltages, power supplies, and test pulse distribution. The front-end hardware can be monitored with the help of suitable online histograms. However, it is essential that the proper hardware diagnostic tools exist in order to detect the failure of a particular component as soon as possible. The histogram observation method frequently implies rather substantial delays in discovering a component failure. A hardware sensor can set off an alarm instantly when, for example, a power supply fails.

The slow control system is designed to respond to expert commands from a local console, generate programmed sequences in response to a command issued from the run control, and take corrective actions in the event of an abnormal situation (voltage trips, *etc.*). This requires that the system have its own local processor, a set of readout and control cards to communicate with the appropriate sensors and control devices, and a link to a local area network (LAN) to receive the run control commands.

The slow controls also generate alarm messages to the central error reporting system as well as status reports. Most of these messages can be handled through the LAN, but some alarms—the hazardous gas monitors, for example—will act on specified hardware interlocks. A link is also required to a database containing the mapping for the physical channels, the calibration constants, and, if required, some voltage or current limits for a channel.

High Voltages. The sense wires, nominally at ~2 kV, will be monitored for the current they draw. The slow control system provides fast ramp-up and ramp-down of voltages. The field wires, maintained at ground potential, do not require monitoring except in the case of small bias voltages for the axial-stereo design.

Low Voltages and Currents. The slow control system will also be used to monitor the voltages and currents in the preamplifiers and the local CAMAC, VME, and VXI crates. This will be achieved with slow 64-channel ADCs having individually programmable gains and differential inputs. About 150 channels are required for the front-end crate power supplies, and about 450 to monitor each preamplifier card, assuming 32 channels and two voltages per card.

Temperature, Pressure, and Gas Flow. The same slow ADCs will be used to monitor ambient temperatures and pressures at various locations and the response from a gas gain monitor. Air flow switches will be handled with parallel input registers.

All of the above controls can be realized using commercial CAMAC modules controlled by a VME processor via a standard A2 CAMAC controller and a VME CAMAC branch driver.

Slow Control via Data Monitoring. The performance of all cells will be monitored locally by histogramming of hits in each cell, track segment density, amplitude and time distributions, and other relevant distributions. These histograms are inspected either visually or, in some cases, automatically if the shape can be compared to a template histogram.

5.9.3 Monitoring

The slow controls described above provide one means of monitoring gas properties such as drift velocity as a function of electric field, the gas gain at the operating point of the chamber, the composition and purity of the gas, and the level of contaminants (such as O_2 and H_2O), which could influence the operation of the chamber. In addition, the quality of incoming premixed gas bottles will be monitored by small test chambers before being introduced to the gas system.

The gas flow and the relative pressures and temperatures must be monitored at various locations for proper operation of the chamber, since the drift time and gas gain depend on the gas density. The chamber pressure is expected to follow the ambient pressure, which fluctuates by $\pm 4\%$ for this geographical region. These pressure differences will affect the chamber gain and drift velocity. The gain can be corrected by applying a scale factor to the pulse height measurements. The drift velocity poses a more difficult problem, since the gas is nonsaturated. Corrections to the track position measurements depend on the distance from the sense wire, and range by at least a factor of 5 over the cell. The SLD experiment measured a 2% change in drift velocities due to ambient pressure fluctuations, which were corrected to 0.2%. The effects of the pressure on the drift velocity are being investigated using the Prototype I chamber. Simulations will be used to determine the best parameterization for the correction.

Monitoring some gas properties inside the chamber would be also advantageous. A laser calibration system is being considered for measurement of the drift time in the chamber volume by ejecting electrons into drift cells through photoemission from field wires using a high-intensity UV laser. The laser beam is transmitted to the chamber via optical fibers. A beam port into the chamber volume will be situated near the midpoint of the outside wall. This arrangement is compact, with few optical elements, such as a small mirror and lens, required to direct the beam transverse to the field wires. The fiber would lie along the outside surface of the chamber with the beam directed into the chamber at 90° by a 45° mirror. The feasibility of this approach will be determined as part of the prototype program.

5.10 Integration

5.10.1 Overall Geometry and Mechanical Support

The mechanical envelope for the drift chamber is shown in Figure 5-2. The envelope includes the space needed for endplates and front-end electronics in addition to the active detector volume. It does not include the volume needed for mechanical supports or cable routing.

The method for supporting the drift chamber is still under study. In one scenario, the chamber is held from the accelerator pedestal in the backward direction and the support tube column in the forward direction. This arrangement allows the support tube to be repositioned (by remote-control cams at each end) or removed independently of the drift chamber. The supports are fastened to the lower edge of the inner radius of each endplate. In another scenario, the chamber is held at its outer radius by the barrel IFR.

5.10.2 Cable Plant and Utilities Routing

The cables and utilities that must be brought into the drift chamber from outside the detector include signal, high voltage, and preamplifier power cables; calibration and monitoring signals; drift gas; and preamplifier cooling gas. All connections are made to the backward endplate, except for gas lines and monitor signals which will be at both ends.

The cross-sectional area and mass are dominated by the signal and HV cables. The cable routing scheme has been laid out assuming 9100 cables of 2.3 mm diameter (signal, monitoring, calibration, and preamplifier power) and 220 cables of 5 mm diameter (HV). The 2.3 mm is approximately the size of RG-174; the actual cables used are likely to be smaller and fewer. Including an additional safety factor of 2, the total cross sectional area reserved for cables is 866 cm^2. The cables and gas lines will be brought into the detector along 2.5 cm-deep cable trays that cover approximately 70% of the inner radius of the DIRC support tube (*i.e.,* at the outer radius of the drift chamber).

The total cable run to the electronics room is approximately 35 m. If thicker cable is needed to preserve signal quality, a transition box will be located close to the detector.

5.10.3 Access

Access to the drift chamber will be needed to replace failed HV capacitors or preamplifiers, to fix gas leaks, and to replace broken wires. None of this is anticipated to be a frequent occurrence. For example, similar front-end electronics have been used on OPAL chambers for seven years without access. In that time, only one of 400 cards has failed. This reliability is achieved both by design—including diode transient suppressors, for example—and by a thorough program of pre-installation testing. A small, randomly distributed number of failed preamplifier cards will have negligible impact on the detector performance. Two HV capacitors will be used in series on each sense wire to improve the reliability of the HV distribution.

A broken wire is a more significant problem than a failed preamplifier. The proposed R&D program will ensure that deformation of the feedthrough and wire due to crimping is understood and will establish the allowed range of crimping force. The crimping tools will be repeatedly calibrated throughout the chamber stringing to ensure operation within this range. With careful attention to such details and a testing period of several months following stringing, experiments such as SLD and BNL-787 have built drift chambers with large numbers of aluminum wires without incurring a single wire break during operation. Tests performed at SLAC indicate that broken wires tend to curl up at the feedthrough rather than fall into the rest of the chamber.

Although regular access will not be required, access procedures have been developed for both ends of the drift chamber. In the forward direction, the endcap-instrumented flux return is vertically split and can be withdrawn along rails at an angle relative to the beam line.

Temporary scaffolding may then be installed, giving very good access to the drift chamber endplate.

In the backward direction, the DIRC support cylinder and water tank create a tunnel containing the Q1, Q2, and Q4 magnets, pumps and masks, flux return iron, and the drift chamber cable trays. For approximately 70% of the azimuthal angle, the return iron can be withdrawn on rails mounted on the support cylinder. After clearing the DIRC water tank, they are then removed by crane.

The time needed to achieve access will be one shift for either endplate. The reassembly time will be longer by approximately one shift for the forward endplate because of the extra time needed to realign the forward calorimeter.

5.10.4 Integration Aspects of the Gas System

The drift chamber has two gas systems, the drift gas ($He:C_4H_{10}$, for example) and the dry nitrogen used to remove the 35 W produced by the preamplifiers. Work is currently underway to establish the flammability of each of the drift gases under study. If necessary, the rf-shield at each endplate can be used to make a second gas seal. This volume would then be flushed by nitrogen to ensure that a flammable concentration of gas cannot accumulate due to a leaking feedthrough. (In the backward direction, nitrogen is also the cooling gas.) In particular, the nitrogen gas distribution will be designed to ensure that a flammable concentration cannot accumulate between the feedthroughs and the printed circuit boards mounted on them. The exhaust gas and a gas sample pumped from the endplate region will both be monitored for oxygen and isobutane concentration. Fire-retardant cables are required in any event as a fire safety measure for the detector.

A large leak of helium could damage the DIRC or aerogel photomultiplier tubes. In addition to the precautions listed above, the photomultiplier tubes may need to be located in a gas-tight volume.

5.10.5 Installation and Alignment

The drift chamber is installed after the magnet, IFR, calorimeter, and DIRC. The machine components from Q2 to Q4 are absent, but the accelerator pedestal is installed in the backward direction. The drift chamber is inserted from the forward end along a beam passing through the chamber to the accelerator pedestal. The forward support tube column is then installed and the drift chamber connected to its permanent supports.

There is an assembly tolerance of 15 mm between the chamber inner radius and the accelerator support tube outer radius. This clearance also allows the remote movement of the tube, which may be as much as 5 mm.

An optical alignment will be performed after the accelerator support tube has been installed in order to place the drift chamber to within 1 mm, and to align the axis of the chamber to within a few mrad. The final, precision alignment will be extracted from data.

5.11 R&D Using Prototype Drift Chambers

Simulation and prototyping efforts are underway in the areas of cell geometry, orientation, layer packing, pattern recognition, and track reconstruction. Several stand-alone data analysis packages are being used, and there have been recent advances on the incorporation of the drift chamber into the BBSIM GEANT package. Prototype efforts are continuing at SLAC, with the current prototype, Prototype I, and further prototyping efforts are being planned.

5.11.1 Prototype I Chamber

A small-cell prototype chamber has been built and is being used to study electrostatic stability, feedthrough design, front-end electronics, cell crosstalk, and wire and gas properties. The prototype is 2.5 m in length, with flat aluminum endplates, 72 anode wires of 20 μm-diameter gold-coated tungsten, and 512 cathode wires of 55 μm-diameter unplated aluminum 5056. The wires are arranged into three superlayers of hexagonal cells with the center superlayer positioned at a 50 mr stereo angle.

Studies of suitable helium-based drift gases are continuing with Prototype I, using cosmic ray particles. To date, the three component gas mixture He:CO_2:C_4H_{10} (83:10:7) and the two component gas mixture He:C_4H_{10} (80:20) have been investigated. Preliminary results are included in Figure 5-14, along with measurements from previous gas studies [Cin91, Pla92, Uno93]. Plans are underway to study other gas mixtures, including He:C_3H_8 and He:C_4H_{10} with lower partial pressures of isobutane. The possibility of including CF_4 as an additive to counter aging is being considered.

Prototype I has also been the test bed for a study of the achievable position resolution using a FADC sampling system and a low-density helium-based gas with pronounced discrete clustering. Data from four anodes, sampled with 8-bit resolution at 250 MHz ($\simeq f_{accel}$), have been artificially compressed to 125 MHz ($\simeq f_{accel}/2$) and 83.3 MHz ($\simeq f_{accel}/3$), and several algorithms for extracting the timing information have been applied to the signals. The results are steadily improving under refinement of these algorithms and currently show single wire position resolutions of 127 μm (at 125 MHz) and 134 μm (at 83.3 MHz) for the gas mixture He:C_4H_{10} (80:20). These should be compared to the single wire resolution of 109 μm obtained with a discriminator and TDC (500 ps bin size). The timing algorithms have yet to be fully optimized, and so further improvements in these values are possible. In early 1995, the preamplifiers of Prototype I will be replaced by ones of a better design, and all 72 channels will be instrumented with 100 MHz FADCs. The Prototype I chamber will then provide full tracking with FADCs.

5.11.2 Prototype II

A second full-length prototype, Prototype II, will be constructed in 1995 and will incorporate all design decisions made to date. It will have sloped carbon fiber endplates, the new crimp-style feedthroughs, and gold-coated aluminum cathode wires.

The preamplifier electronics for this chamber will be furnished by UCSC, in the form of an ASIC with adjustable gain, rise time, and shaping time. This preamplifier will allow precise determination of the characteristics of the final preamplifier design in accordance with the chamber cell response and the timing algorithm used. Cell shape, aspect ratio, layer arrangement, and the segmentation of high voltage, power, and calibration signals will reflect the decisions of the group with respect to the internal chamber geometry.

5.11.3 Other R&D Efforts

Depending upon the availability of a test beam, a somewhat smaller test chamber could be used for dE/dx studies. It would also be desirable to use such a chamber for studies of tracking, dE/dx, and Lorentz angles in helium-based gas mixtures in the presence of a magnetic field.

Studies on the aging of the drift gas in a high rate environment are underway at TRIUMF and at LBL. The most likely gas candidates, as identified in the Prototype I studies, will be subjected to long term aging tests. The usefulness of CF_4 as a gas additive to counter aging will be investigated as well.

References

[Bia89] The MAGBOLTZ Simulation Code was kindly supplied by S.F. Biagi of the University of Liverpool. Some results from this code are discussed in S.F. Biagi, *Nucl. Instr. Methods* **A283**, 716 (1989).

[Boy92] A. Boyarski, D. Briggs, and P. Burchat, *Nucl. Instr. Methods* **A323**, 267 (1992).

[Bra94] D. Brashford *et al.,* "The Use of High Stiffness Material and Dimensionally Stable Materials in Spacecraft Applications," in Proceedings of the Int. Workshop on Advanced Materials for High Precision Detectors, CERN 94–07, p. 9 (1994).

[Bri93] D. Britton and E. Hyatt, "Pattern Recognition in an All Stereo Drift Chamber," *BaBar Note* # 102 (1993).

[Cin91] V. Cindro *et al., Nucl. Instr. Methods* **A309**, 411 (1991).

[IM7] Manufactured by ICI Fiberite, Tempe, AZ.

[Inn93] W. Innes, "TRACKERR, A Program for Calculating Tracking Errors," *BaBar Note* # 121 (1993).

[Pla92] S. Playfer *et al., Nucl. Instr. Methods* **A315**, 494 (1992).

[RAD] Manufactured by Dupont.

[Smi94] C. Smith, McGill Internal Technical Memo, McG–BF–TM–0007, (1994).

[Uno93] S. Uno *et al., Nucl. Instr. Methods* **A330**, 55 (1993).

[Vav82] J. Va'vra, L. Roberts, D. Freytag, and P. Clancey, *Nucl. Instr. Methods* **A203**, 109 (1982). The code has been modified to use the number of primary ions in the calculations.

[VIT] Manufactured by ICI Advanced Materials, Exton, PA.

[You89] W.C. Young, "Roark's Formulas for Stress and Strain," 6th Edition, McGraw Hill, (1989).